Materials & Design 266 (2026) 116152

Contents lists available at ScienceDirect

Materials & Design

journal homepage: www.elsevier.com/locate/matdes

Microstructure-informed creep model for 30CrMoNiV11-5 steel

Fan Chen [a,*,1], Rojas-Ulloa Carlos [a,1], Jérôme Tchoufang Tchuindjang [b], Olivier Dedry [b], Rishabh Bharadwaj [c], Mahesh Somani [c], Anne Mertens [b], Anne Marie Habraken [a]

[a] Materials and Solid Mechanics, University of Liège, Quartier Polytech 1, Allée de la Découverte 9 B52/3, 4000 Liège, Belgium
[b] Metallic Materials Science, University of Liège, Quartier Polytech 1, Allée de la Découverte 13 B52/3, 4000 Liège, Belgium
[c] Materials and Mechanical Engineering, Centre for Advanced Steels Research, University of Oulu, P.O. Box 4200, FI-90014 Oulu, Finland

ARTICLE INFO

Keywords:
30CrMoNiV11-5 steel
Creep deformation
Mean-fieldcreepmodeling
Dislocation dynamics
Microstructural characterization

ABSTRACT

30CrMoNiV11-5 is a high-strength rotor steel used in turbine shafts, where creep governs long-term performance under elevated temperature and stress. In this work, a physics-based mean-field creep (MFC) framework is developed, in which dislocation populations (mobile, immobile, and boundary) are coupled with precipitate-kinetics inputs and damage evolution arising from precipitate coarsening and cavitation. The precipitate state is obtained from thermo-kinetic simulations based on the alloy heat-treatment history. The model is calibrated against 7 standard creep tests at 550 °C over a stress range of 283–450 MPa. It successfully reproduces the primary–secondary–tertiary creep behaviour, captures the stress dependence of the minimum creep strain rate, and predicts rupture time with good fidelity. The predicted microstructural evolution is consistent with TEM and EBSD observations, and the model allows analysis of the respective roles of intragranular and boundary-related precipitates. The proposed framework provides a mechanism-based approach for creep-life assessment of 30CrMoNiV11-5 and related rotor steels.

1. Introduction

Large turbine shafts made of high-strength, heat-resistant steels such as 30CrMoNiV11-5 operate for years under elevated temperatures and substantial mechanical loads, where creep— the time-dependent plastic strain that develops even below the macroscopic yield stress—can become life-limiting [1]. The manufacturing route for such shafts is long and complex (casting and forging, controlled cooling, normalizing and tempering, machining, quenching and re-tempering, and stress-relief heat treatment), which invariably raises the cost of late discovery of inadequate creep resistance [2,3]. Direct experimental verification of creep performance is rarely feasible in real time scale, as rupture times can span over several years, even beyond 10 years. Besides, laboratory reproduction of service conditions is slow and resource-intensive, and hence, results are prone to be sensitive to environmental fluctuations and instrumental drift (temperature/stress oscillations, sensor aging and calibration error, etc.) [3]. Moreover, microstructural evolution (dislocation recovery/subgrain growth, precipitates coarsening, cavity nucleation at boundaries) governs the response and underlines life-assessment practice in rotor steels [4,5]. Consequently, reliable pre-deployment prediction of creep life is essential to avoid costly material, energy, and economic waste. These constraints motivate the development of an accurate, physics-based numerical model that can infer long-term creep behaviour from shorter-term tests and microstructural information.

Classical phenomenological approaches relate creep response to temperature and time through regressions—power-law (Norton–Bailey) fits for minimum rate and parametric master-curve methods such as the Larson–Miller parameter (LMP) for rupture—so that short tests can be projected to long-term service [6–8]. These tools reduce test burden, but invariably rely on time–temperature equivalence and on fitted "constants" that, in practice, vary with stress, temperature, and metallurgical history; extrapolations thus become method-dependent rather than mechanism-anchored [9]. Comparative studies on Cr-bearing martensitic steels show that different phenomenological reductions yield divergent long-term predictions and are revised as additional data accrual, underscoring limited transferability across regimes [10]. For cyclic creep–fatigue service, Morch proposed a phenomenological viscoplasticity framework for receiver tubes in concentrated solar power plants, built on a Chaboche-type model, calibrated to thermo-

* Corresponding author.
E-mail address: fanchen@u.nus.edu (F. Chen).
[1] Equal contributions.

https://doi.org/10.1016/j.matdes.2026.116152
Received 21 December 2025; Received in revised form 24 April 2026; Accepted 28 April 2026
Available online 2 May 2026

mechanical tests, and intended for lifetime prediction [11]. Nevertheless, like related approaches, it does not resolve explicit microstructural state variables (e.g., precipitate radii/densities, subgrain size), which limits mechanism-consistent extrapolation. Continuum-damage formulations developed in the same manner add degradation variables, but are prone to damage localization (and mesh sensitivity) in tertiary creep unless regularized, which undermines predictive robustness [12,13]. Recent accelerated-testing and re-parameterization schemes (e.g., Wilshire-type approaches and stepped-isostress protocols) improve data efficiency, yet remain as curve-fitting surrogates tied to stress–temperature regressions rather than to evolving microstructural variables [14,15]. These limitations motivate a mechanism-based framework in which creep strain rate and rupture emerge from explicitly evolving microstructure, i.e., dislocation populations, subgrain evolution, precipitate kinetics, and damage, rather than from parametric extrapolation alone.

Recent data-driven efforts have sought to improve creep predictions by learning stress–temperature–composition mappings from compiled datasets. Some studies report accuracy gains by transforming the target with time–temperature parameters (e.g., LMP/ Manson–Haferd Parameter/ Manson–Succop Parameter) and training regressors on those transformed labels, which stabilizes fits but retains the parametric character of the extrapolation [16]. Others pursue explainable formulations, e.g., linear-independent-descriptor regression, to derive analytical expressions for rupture time over multi-steel datasets, yet the performance hinges on carefully curated variables and consistent protocols [17]. For Cr-bearing martensitic steels, machine learning (ML) frameworks (Support Vector Regression/Random Forest/Gradient Boosting Decision Trees, ensembles, Gaussian processes) interpolate well across mixed heats and can rank influential factors; nevertheless, generalization degrades across product forms or microstructural states unless additional descriptors (such as proof stress at the test temperature) are supplied [18–20]. In practice, ML also depends on accurate, sizeable databases, whereas assembling creep datasets experimentally is inherently slow and heterogeneous across laboratories; training is therefore data-limited and sensitive to protocol variability. In this setting, a reliable physics-based model can generate curated synthetic data and serve as a prior serve to regularize learning under scarcity. Finally, most published ML studies target rupture time or minimum rate rather than the full three-stage creep trajectory with internal variables, which limits comprehensiveness for life assessment [21].

For 30CrMoNiV11-5, publicly available microstructure-resolved datasets are limited; nevertheless, sources from closely related rotor-steel grades provide informative constraints. Hardness profiles measured on DIN 1.6946 welds and heat-affected zones after multi-pass submerged arc welding and post-weld heat treatments provide constraints on the tempering response and on property gradients expected across rotor sections [22]. Creep-ductility investigations on 1CrMoV rotor steels delineate transitions between ductile and cavity-controlled fracture, informing failure modes and notch sensitivity under service-relevant conditions [23]. At the component scale, operational transients (e.g., start-ups) have been shown to consume rotor life, underscoring the need to couple materials response with duty cycles in life assessment [24]. Methodologically, probabilistic lifetime frameworks and damage-evolution studies for high-Cr steels, including cases involving DIN 1.6946/SEW 555, illustrate how uncertainty can be propagated and how degradation variables are inferred, although the constitutive cores are largely phenomenological [25,26]. By contrast, consolidated, time-aligned datasets for 30CrMoNiV11-5 that link creep curves with dislocation/subgrain metrics and site-resolved precipitate coarsening and transition to stabler forms are scarce. Available compilations are often cross-alloy or emphasize data-fusion/ML without the internal variables required to test mechanisms directly [27]. Related work on microstructure evolution (e.g., phase-field studies) highlights the need to connect kinetics to macroscopic response, but it has not yet been integrated for this alloy to enable prediction across the full three-stage creep trajectory [28].

Given these limitations and the scarcity of microstructure-resolved data for 30CrMoNiV11-5, a framework that connects creep strain to the evolving dislocation and precipitate states, and their interactions, is required. A mean field, dislocation-based approach provides this link. Mean field, dislocation-based creep modelling originates with Ghoniem's framework, which treats creep as Orowan-type plastic flow governed by the coupled evolution of mobile, static, and boundary dislocation populations, together with subgrain formation and obstacle fields, while the rate kinetics reflect glide and diffusion-controlled climb [29]. For tempered-martensitic steels, later hybrid formulations coupled the mean field core to continuum damage so that precipitate coarsening and cavity formation soften the effective resistance and drive tertiary creep. These models deliver full creep curves and internal variables such as dislocation densities, effective stress, and subgrain size, and have been benchmarked against P92/P9x datasets [30]. More recent work incorporated precipitate-kinetics inputs (radius and number-density classes) for P91, yielding creep curves and rupture trends consistent with repository data while tracking subgrain and dislocation trajectories [31,31]. In parallel, applications to Ni-based Alloy 617 combined dislocation creep with diffusion creep at low stress and introduced damage laws calibrated to ductility measures, improving life predictions while preserving microstructural consistency [32,33]. These developments rely on characterization routes that quantify the state variables evolved by the models, including EBSD and X-ray line-profile methods to determine dislocation density in lath martensite and to parameterize subgrain metrics [34], studies of subgrain coarsening under creep or cyclic loading in 9–12 %Cr steels [35], and carbide-precipitation analyses that inform precipitate classes and Zener-pinning terms in CrMoV steels [36]. Collectively, this body of work establishes a transferable mean field toolkit in which Orowan kinematics, mechanism-informed kinetics, precipitate coupling, and damage provide a coherent basis that can be adapted.

The current study develops and validates a mechanism-based mean field creep (MFC) model for 30CrMoNiV11-5. Prescribed stress–temperature histories drive a constitutive core taking into account both dislocation- and diffusion-creep mechanisms. Mobile, static, and boundary dislocation populations with dynamic and static recovery are explicitly coupled to precipitate kinetics (site-resolved radius and number-density histories). As shown in Fig. 1, a damage module for cavity nucleation and growth together with coarsening-induced softening completes the microstructural block. The coupled equations are implemented in JAX [37], a NumPy-like Python library that provides automatic differentiation and just-in-time compilation via XLA (Accelerated Linear Algebra) to CPU/GPU. They are solved by a Newton method using auto-differentiated Jacobians. Adjustable parameters are identified by optimization against standard creep tests (SCT), producing a closed modelling–experiment loop. The framework outputs full creep curves, minimum-rate trends, damage evolution, and rupture time. It reproduces primary–secondary–tertiary behaviour and the stress–temperature dependence of the minimum rate. The model also returns microstructural trajectories consistent with EBSD observations. To address residual low-stress discrepancies, a small baseline creep-rate term consistent with diffusion-accommodated deformation is included. Overall, the model provides a transferable basis for creep-life assessment in 30CrMoNiV11-5 and related rotor steels.

While several mean-field creep models have been proposed for high-temperature steels and Ni-based alloys, including the work of Riedlsperger et al. for P91 and Alloy 617, their application to rotor steels such as 30CrMoNiV11-5 remains limited. The present work adapts this framework to rotor steel conditions and introduces several additional elements. In particular, the precipitation state is identified through thermodynamic and kinetic simulations based on the alloy heat treatment. The new MFC model parameter evolution reveals a transition window separating diffusion-assisted and dislocation-dominated creep regimes. Sensitivity analyses are also performed to clarify the role of

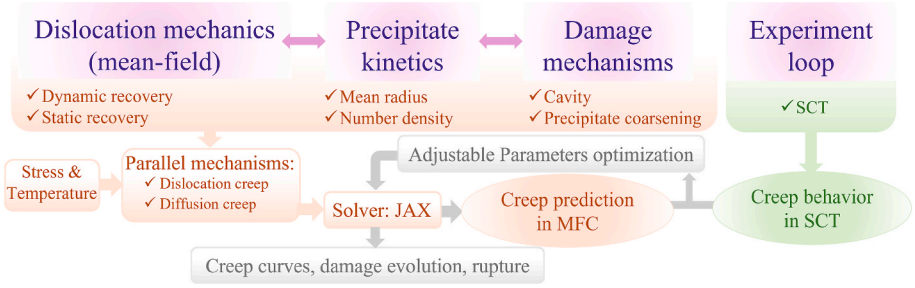

Fig. 1. Schematic of the developed physics-based mean-filed creep (MFC) model and its validation pipeline.

grain size and nucleation sites in controlling creep hardening and damage evolution.

2. Material and creep phenomenon

2.1. Material characteristics

The alloy studied is 30CrMoNiV11-5, also standardized as DIN 1.6946 / SEW 555. Historically, 1CrMoV was the first rotor steel for large steam turbines. Subsequent deployments featured 26CrMoNiV3-8 in the UK and 30CrMoNiV5-11 with mainland European manufacturers after the 1990 s [23]. 30CrMoNiV11-5 was selected in the present study not because it represents the most advanced rotor alloy for the newest ultra-supercritical units, but because it remains an industrially relevant forged rotor-shaft steel for power-generation applications and was available with a representative manufacturing and heat-treatment history. This makes it particularly suitable for developing and validating a microstructure-informed creep framework in which both the initial microstructural state and the subsequent precipitation evolution must be defined consistently. In addition, the alloy exhibits a heterogeneous bainitic/ferritic matrix with multiple carbide families, so it constitutes a challenging rather than simplified case for mechanism-based creep modelling.

The chemical composition of the present alloy is given in Table 1. The material was produced following the established elaboration route: casting, forging, controlled cooling, normalizing and tempering, machining, water quenching and re-tempering, followed by stress-relief operation.

Microstructural characterization of the heat-treated material indicates a predominantly bainitic matrix with a minor ferritic fraction. Representative SEM observations at different magnifications are shown in Fig. 2(a–c), where the bainitic morphology and lath/packet features are clearly visible. After tempering, carbide precipitation is observed both within the matrix and along grain boundaries, as illustrated by the SEM image in Fig. 2(c). TEM observations further confirm the presence of dispersed precipitates in the heat-treated material (Fig. 2(d–e)). The corresponding EDS maps in Fig. 2(f–g) show Cr-rich and Mo-rich regions associated with representative particles, consistent with the presence of carbide precipitates considered later in the precipitation modelling and creep framework.

Creep tests were conducted at 550 °C under nominal stresses varying in the range 283 to 450 MPa. The detailed microstructure inputs used in the MFC model are provided in Section 4.

2.2. Standard creep test

Uniaxial tensile creep tests were performed on a Zwick Roell Kappa 100 DS with constant-load and temperature in accordance with ISO 204 [38]. The machine operates in closed-loop load control using a base-mounted force transducer and a rigid crosshead. SCTs were conducted at constant nominal stress and a fixed temperature, following the standard sequence of specimen alignment, thermal soak, load application. A continuous acquisition of force, temperature, and displacement is applied with a frequency of 0.0083 Hz. Thermocouples (N-type) were welded to the gauge section to monitor and control specimen temperature. Axial displacement was recorded by high-temperature displacement sensors mounted on a ceramic frame (Fig. 3). The frame was attached to the two raised rings at the specimen ends, defining a 50 mm gauge length and reducing furnace-compliance effects. The force sensor at the base of the frame supplied the feedback signal for load control.

After mounting and alignment, the specimen was heated under a small initial preload (seating load) to ensure proper contact and alignment, and held for 1 h to reach thermal equilibrium. The target stress was then applied and maintained for the duration of the test through closed-loop load control, in which the force transducer continuously adjusted the actuator to compensate for strain-induced load changes. Tests were conducted at 550 °C with nominal stresses in the range of 283–450 MPa. Engineering strain was computed from the displacement over the 50 mm gauge length. The minimum creep strain rate was ascertained from the strain–time record using a sliding-window linear fit centred on the secondary regime. Rupture time was defined as the time to fracture; for unfailed specimens the test was stopped after a prescribed duration, and the last valid minimum-rate estimate was retained. Conformity with ISO 204 was verified by checks of alignment, calibration of load and displacement channels, and thermal stabilisation. Potential sources of error, including thermal gradients, long-term sensor drift, and fixture compliance, were mitigated by multiple thermocouple monitoring, soak periods, and the fixed 50 mm gauge-length extensometry.

2.3. Creep deformation mechanisms

Creep in 30CrMoNiV11-5 proceeds through two concurrent routes. Over most of the service window (high stress, high temperature) the strain rate is governed by dislocation creep, in which dislocations glide between obstacles and advance by diffusion-assisted climb when they encounter barriers. In the mean field description, this behaviour is expressed through an Orowan-type relation that links strain rate to the product of the Burgers vector, the mobile dislocation density, and the average dislocation velocity, with the latter controlled by the local

Table 1
Chemical composition of 30CrMoNiV5-11 (wt%).

C	Si	Mn	Cr	Mo	Ni	V	Cu	S	P
0.28	0.10	0.65	1.37	1.08	0.63	0.29	0.10	0.01	0.009

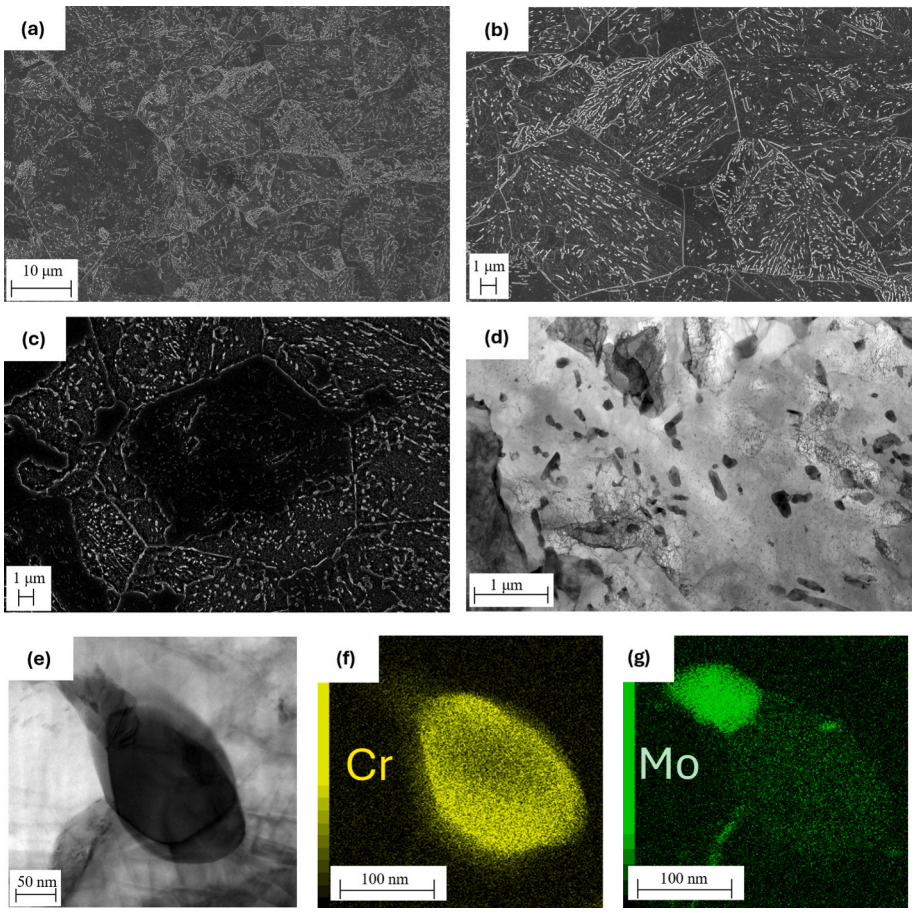

Fig. 2. Microstructural characterization of the heat-treated 30CrMoNiV11-5 steel. (a–b) SEM images at different magnifications showing a predominantly bainitic microstructure with lath/packet features. (c) SEM image after tempering indicating carbide precipitation both within the matrix and along grain boundaries. (d) TEM overview showing dispersed precipitates in the heat-treated matrix. (e) High-magnification TEM image of a representative precipitate. (f–g) Corresponding EDS elemental maps showing Cr-rich and Mo-rich regions associated with the precipitate.

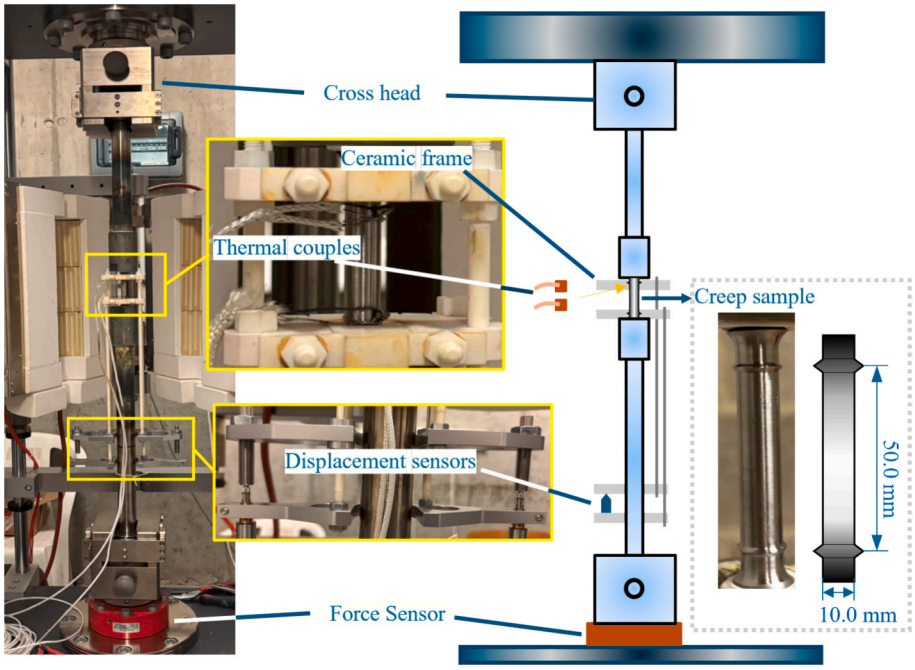

Fig. 3. Creep setup (Zwick Roell Kappa 100 DS): cross head and load train, ceramic frame with displacement sensors attached to specimen rings, welded thermocouples on the gauge, and base-mounted force sensor.

stress, temperature, and obstacle field [29]. At low stresses and high temperatures, the diffusion creep contribution becomes non-negligible, accommodated by lattice and grain-boundary diffusion and scaling with diffusivity and an effective structural length such as the grain or subgrain size [31–33].

Fig. 4 sketches the mechanism picture at the scale of a grain fragment. Mobile dislocations populate the subgrain interior, while static dislocations and boundary dislocations accumulate at subgrain and grain interfaces. Precipitates occur both inside bainitic laths and on boundaries. Vacancy and atom fluxes facilitate climb processes and recovery, with sinks located at boundaries, precipitates, and interfaces. The substructure is represented by a network of subgrain boundaries with a characteristic radius R_{sgb}, and the outer grain boundary with radius R_{gb} bounds the domain. Under an applied stress the mobile dislocations glide until they are arrested by obstacles; subsequent climb, driven by vacancy flux to jogs, permits bypass and sets the steady component of the creep rate.

The evolution of the internal structure governs the transition between creep stages. Immobilization converts mobile dislocations to static populations, while dynamic recovery removes paired dislocations during glide. Static recovery annihilates dipoles during climb. These processes reduce the stored dislocation density and promote subgrain growth. Carbide precipitates, such as $M_{23}C_6$ on boundaries and VC or V(C,N) inside laths, pin interfaces and limit the mean free path. Their coarsening reduces pinning, accelerates recovery, and changes the effective structural length that enters both dislocation and diffusion creep formulations. Later, cavities preferentially nucleate at boundaries, inclusions, and coarse intergranular carbides. Their growth reduces the load-bearing area and accelerates the approach to tertiary creep and rupture. The state variables used within the MFC model include the mobile, static, and boundary dislocation densities; the subgrain size; precipitate radius and number density for each site. A scalar damage variable reflects cavity evolution. These variables represent the microstructure state linked to the observed primary, secondary, and tertiary response of the alloy [29,31–33]. The constitutive equations that realize this mechanism-based description, together with the numerical treatment, are presented in Section 3.

3. Constitutive law

This section formulates the governing equations for creep in 30CrMoNiV11-5. It defines the internal variables, and specifies how dislocation creep, diffusion creep, precipitate kinetics, and damage are coupled. We begin with the mean field framework for dislocation-controlled creep and its modified Orowan relation, then describe kinetics for glide and climb and the evolution of mobile, static, and boundary dislocation densities. We add a Coble-type grain-boundary diffusion-creep term, while lattice diffusion is accounted via the dislocation-climb kinetics, and damage variables represent precipitate coarsening and cavitation. The complete set of equations yields the total creep rate used in the simulations, while Section 4 details parameter identification, numerical implementation, and validation.

3.1. Mean field creep model

The MFC framework provides a physics-based description of time-dependent deformation by linking the macroscopic creep strain rate to the averaged microstructural quantities. Unlike empirical power-law or other phenomenological functions, MFC is grounded in dislocation mechanics and precipitate kinetics, so it captures the competition between strain hardening and recovery that controls long-term creep. The formulation originates from Riedlsperger's dislocation-based framework, which has been refined and validated for martensitic steels and Ni-based alloys [33].

3.1.1. Modified Orowan equation

At its core, the macroscopic creep strain rate is expressed through a modified Orowan relation [29]:

$$\dot{\varepsilon}_{disl} = \frac{b\rho_m v_{eff}}{M} \tag{1}$$

where b is the Burgers vector, ρ_m is the mobile dislocation density, M is the Taylor factor, and v_{eff} is the effective dislocation velocity that combines glide and climb phenomena.

3.1.2. Effective dislocation velocity $\boldsymbol{v_{eff}}$

Glide v_g and climb v_c velocities act in series with respect to obstacle bypass, so the effective velocity is taken as a harmonic combination [33],

$$\frac{1}{v_{\mathrm{eff}}} = \frac{1}{v_g} + 2\pi\left(\sum r_{p,i}^3 N_{p,i}\right)\cdot\frac{1}{v_c} \tag{2}$$

where $r_{\mathrm{p},i}$ and $N_{\mathrm{p},i}$ are the mean radius and number density of precipitate population i. A larger precipitate content reduces v_{eff}, representing strengthening by reduced spacing.

3.1.3. Glide velocity $\boldsymbol{v_g}$

Glide motion is treated as a thermally activated process governed by the applied stress, internal stress, and an activation volume [39]:

$$v_g = a_1 \exp\left(\frac{-Q_{self}}{k_B T}\right)\exp\left(\frac{-\sigma_{\mathrm{i}} V_{\mathrm{r}}}{k_B T}\right) 2\sinh\left(\frac{\sigma_{app} V_{\mathrm{r}}}{k_B T}\right) \tag{3}$$

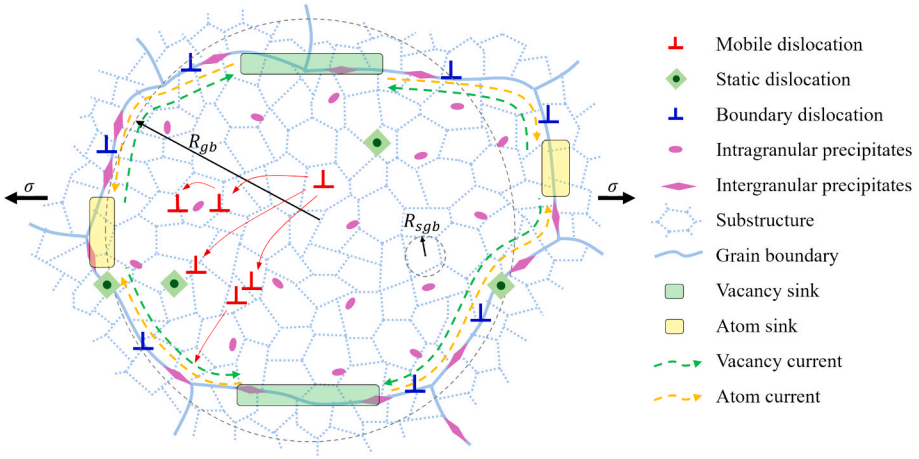

Fig. 4. Generic deformation mechanisms for mean field creep model.

where a_1 is a pre-exponential factor, Q_{self} is the self-diffusion activation energy, V_r is an activation volume, k_B is Boltzmann's constant, while σ_{app} and σ_i are the applied and internal stresses. T is the absolute temperature. The internal stress is given by a Taylor-type relation [40]:

$$\sigma_i = \alpha M G b \sqrt{\rho_m + c_s \rho_s} \tag{4}$$

here, G is the shear modulus, ρ_s the static dislocation density and α the dislocation-interaction coefficient. The coupling factor c_s specifies the contribution of static dislocations to the internal stress. The term $\rho_m + c_s\rho_s$ therefore represents the effective forest-dislocation density acting as obstacles to mobile dislocation glide.

3.1.4. Climb velocity v_c

Dislocation climb enables recovery and bypass of obstacles through diffusion of vacancies. Both lattice diffusion and pipe diffusion along dislocation cores are considered [29]. The climb velocity is taken as the sum of two contributions: the lattice-diffusion component v_{cl} and the pipe-diffusion component v_{cp}:

$$v_c = v_{\text{cl}} + v_{\text{cp}} \tag{5}$$

(a) Lattice diffusion component [31]:

$$v_{cl} = \frac{2\pi\eta_v D_{\text{l}}}{\left[1 - \eta_v \ln\left(L_\alpha \sqrt{\rho_t}\right)\right]} \exp\left(\frac{-\sigma_{\text{i}}\Omega}{k_B T}\right) 2\sinh\left(\frac{\sigma_{app}\Omega}{k_B T}\right) \tag{6}$$

where D_l is the lattice diffusion coefficient, η_v is a geometric constant, L_α is a characteristic length, ρ_t is a total dislocation density, and Ω is the atomic volume. The diffusivity follows $D_l = D_l^0 \exp(-E_{\text{lattice}}/(k_B T))$, D_l^0 is the pre-exponential diffusion constant (the high-temperature limit of the diffusivity) and E_{lattice} is the lattice-diffusion activation energy.

(b) Pipe diffusion component [31]:

$$v_{\text{cp}} = \left\{\frac{2\pi b D_{\text{p}}}{L_p^2}\right\} \exp\left(\frac{-\sigma_{\text{i}}\Omega}{K_B T}\right) 2\sinh\left(\frac{\sigma_{app}\Omega}{K_B T}\right) \tag{7}$$

with pipe-diffusion coefficient D_p. The pipe diffusivity follows $D_p = D_p^0 \exp(-E_{\text{pipe}}/(k_B T))$, where D_p^0 is the pre-exponential pipe-diffusion constant and E_{pipe} is the pipe-diffusion activation energy [41]. The core diffusion length L_p is [42]:

$$L_p = \sqrt{2} a_g \exp\left(\frac{\Delta W}{2 k_B T}\right) \tag{8}$$

where a_g is the lattice constant and ΔW is the vacancy-formation energy.

3.1.5. Dislocation density evolution

Mobile ρ_m, static ρ_s, and boundary ρ_b dislocation densities evolve through multiplication, immobilisation, annihilation, and recovery. A representative set of rate equations is [31]:

$$\dot{\rho}_m = \rho_m\left(\sqrt{\rho_m} + \sqrt{\rho_s}\right) v_g + \frac{\beta \rho_s R_{gb}}{\tilde{h}_1^2} v_g + \frac{\rho_s}{\lambda} v_c + \frac{\rho_s f_v b}{r_p} v_c + \frac{\rho_s}{2 r_p} v_g - \frac{\rho_m}{2 R_{gb}} v_g$$

$$- \frac{\rho_m}{\lambda} v_g - \frac{\rho_m}{h_1} v_g - 8 \rho_m^{\frac{3}{2}} v - \delta_{anh}(\rho_m + \rho_s)\rho_m v_g \tag{9a}$$

$$\dot{\rho}_s = \frac{v_{eff}}{2 R_{gb}} \rho_m - 8 \frac{v_c}{h_b} \rho_s - \delta_{anh} \rho_s \rho_m v_{eff} \tag{9b}$$

and the boundary density ρ_b evolves as [31]:

$$\dot{\rho}_b = 8(1 - 2\zeta)\rho_s \frac{v_c}{h_b} - M_{sb}\left[P_{sgh} - 2\pi\left(\sum_i r_{p,i}^2 \cdot N_{p,i}\right)\gamma_{sgb}\right] \frac{\rho_b}{R_{sgb}} \tag{9c}$$

here, β is the boundary-to-mobile transfer coefficient, R_{gb} is the grain-boundary capture/interaction radius; R_{sgb} is the subgrain-boundary curvature radius; h_1 is the characteristic wall spacing used for emission/capture, λ is the forest mean free path (obstacle spacing), f_v scales climb-assisted precipitate bypass, r_p is the representative precipitate radius in dislocation–particle interactions, h_b is the subgrain-boundary spacing, δ_{anh} is the coefficient for glide-assisted annihilation, M_{sb} is the subgrain-boundary mobility, P_{sgb} is the stored-energy driving pressure for subgrain growth, and γ_{sgb} is the subgrain-boundary energy that appears in the Zener-pinning term.

In Eq. (9a), the first two positive terms—$\rho_m(\sqrt{\rho_m} + \sqrt{\rho_s})v_g$ and $(\beta \rho_s R_{gb}/h_1^2)\tilde{v}_g$—represent Frank–Read multiplication and boundary emission, respectively. Subsequent terms account for immobilisation, storage, climb recovery and annihilation. In Eqs. (9b)–(9c), the leading terms describe storage into the static network and climb-driven wall build-up, respectively. The coupled system captures the balance between hardening and recovery that produces the primary–secondary creep transition.

4. Diffusion-Creep contribution

At low stress and high temperature, a boundary-diffusion–controlled strain rate is added to the dislocation term. The Coble form reads [43]:

$$\dot{\varepsilon}_{\text{diff}} = A_c \frac{D_{gb}\, \delta_{gb}\, \sigma_{\text{app}}\, \Omega}{(2R_*)^3\, k_B T} \tag{9d}$$

where A_c is a geometry factor, D_{gb} is the grain-boundary diffusivity, δ_{gb} is the effective boundary width. The structural length R_* is taken as the subgrain radius R_{sgb} once a stable substructure forms; in the absence of subgrains it reduces to the grain radius R_{gb}. The diffusivity follows an Arrhenius law $D_{gb} = D_{gb}^0 \exp(-Q_{gb}/k_B T)$. where D_{gb}^0 is pre-exponential constant, and Q_{gb} is the grain-boundary diffusion activation energy. Eq. (9d) supplies $\dot{\varepsilon}_{\text{diff}}$ in Eq. (10), so that the total creep rate combines dislocation creep with Coble creep, while damage terms modulate the effective load-bearing capacity.

4.1. Integration of damage evolution

To reproduce tertiary creep and rupture, MFC is extended with precipitate-coarsening damage and cavitation damage, both of which reduce the effective load-bearing capacity. Dissolution and phase transitions are captured implicitly through the TC-PRISMA precipitation-kinetics trajectories supplied to the MFC model. The total creep rate is:

$$\dot{\varepsilon}_{creep} = \left(\dot{\varepsilon}_{disl} + \dot{\varepsilon}_{diff}\right) \frac{1}{\left[(1 - D_{ppt})(1 - D_{cav})\right]^{k_d}} \tag{10}$$

where $\dot{\varepsilon}_{disl}$ and $\dot{\varepsilon}_{diff}$ denote the dislocation-creep strain rate and the diffusion-related creep strain rate, respectively. The former dominates at higher stress levels and is associated with dislocation motion and recovery, whereas the latter represents diffusion-assisted deformation mechanisms that are more significant at lower stresses. D_{ppt} and D_{cav} are precipitate-coarsening damage and cavitation damage. k_d is damage-coupling exponent.

4.1.1. Precipitate-coarsening damage

Following Murchú et al. [44] for 9Cr steels, loss of subgrain-boundary pinning due to coarsening of $M_{23}C_6$ and V(C, N) is described by: $D_{ppt}(t) = 1 - \frac{L_s^0}{L_s(t)}$ (11)

with the mean precipitate spacing L_s and its initial value L_s^0 are calculated according to [45]: $L_s = \sqrt{\frac{2}{3}} \frac{\sum_i N_i r_i^2}{\sum_i N_i r_i}$, $L_s^0 = \sqrt{\frac{ln(3)}{2\pi \sum_i N_i r_i} + (2r_A)^2} - 2r_A$ (12)

where r_i and N_i are the mean radius and number density for precipitate i, and r_A is a reference radius. As coarsening progresses, $L_s(t)$

increases and D_{ppt} approaches unity.

4.1.2. Cavitation damage

Cavity nucleation and growth at grain or subgrain boundaries are represented by a Rabotnov–Kachanov-type law adapted from Murchú et al. [44],$\dot{D}_{cav} = (D_{cav}(t) + a_d(1 + b_d e^{\frac{T}{c_d}}))\dot{\varepsilon}_{creep}$(13)

where a_d, b_d, and c_d are empirical constants. In the present work, this cavitation law is used as an effective strain-driven description within a 1D uniaxial creep framework. It does not explicitly include tensorial stress effects such as stress triaxiality or hydrostatic stress, and is therefore intended to capture the onset and acceleration of tertiary creep rather than the full mechanistic details of void growth under multiaxial loading.

4.1.3. Damage initiation criterion

Damage is activated once a stored-energy measure SE exceeds a threshold [49]:$SE = A\sigma_{app}\left(1+\dot{\varepsilon}_{creep}\right)\dot{\varepsilon}_{creep}^{\frac{1}{m}} \geq SE_{threshold}$(14)

where A is a material-dependent scaling coefficient linking the applied stress to the stored-energy measure SE, and m is an exponent controlling the sensitivity of the stored-energy measure to the creep strain rate. These parameters are identified through calibration against the experimental creep data. After activation, equations (11)–(13) govern the progressive reduction of effective area and the acceleration toward rupture.

5. Model setup

The constitutive framework uses a small set of fixed crystal and elastic inputs, a calibrated group of dislocation-structure parameters, and microstructural trajectories obtained from precipitation modelling and microstructure evolution. These ingredients link operating mechanisms to data and permit one parameter set to span the stress–temperature range considered. The geometric and elastic scales are held constant and comprise the Burgers vector, lattice parameter, and atomic volume together with Young's modulus, Poisson's ratio, and the Taylor factor. They set the shear–to–axial conversion and the spacing/velocity scales entering the Orowan kinematics. Numerical values are listed in Table 2 and are used unchanged in all simulations. The Burgers vector and lattice parameter follow standard bcc iron values [46,47]; Young's modulus and Poisson's ratio are the adopted 550 °C elastic constants [26]; the Taylor factor is the conventional bcc polycrystal value [36]; the atomic volume is calculated from the bcc unit cell (unit-cell volume divided by two atoms per cell).

Hardening and recovery emerge from the interaction of mobile, static, and boundary dislocation populations. The interaction coefficient and mobile–static coupling enter the internal stress, while transfer and geometric factors control emission, immobilisation, and boundary storage. Glide kinetics uses a single pre-exponential factor, and the initial sub-boundary misorientation fixes the starting subgrain radius. The parameters that govern these effects are summarized in Table 3, but the emphasis is on their role, as they regulate the balance between multiplication and recovery of dislocations that sets the primary–secondary creep transition. These parameters are not just fitting the curve at a given condition, which also encompass the temperature range and stress range covered by the model. Parameter calibration began from the reference sets in [31–33], and a restricted subset was then adjusted to match our creep curves at 550 °C.

Most model parameters are not freely fitted, but are fixed either from literature values, direct measurements, or physically motivated estimates, as summarized in Tables 2–5. The calibrated subset is limited to the parameters most directly controlling glide mobility, damage initiation and tertiary acceleration. These calibrated parameters are identified against the experimental creep curves at 550 °C and then assessed over the investigated stress range. In this sense, the parameter set is not intended as a purely numerical fit, but as a constrained identification within a physically informed framework.

Temperature sensitivity enters through the glide activation energy and the vacancy-transport energies for lattice and pipe diffusion. As listed in Table 4, the lattice/pipe values are adopted from the creep/dislocation-transport literature [42]; the glide energy is tuned within those bounds so the model reproduces the measured slope of the minimum-rate trend while keeping a single activation volume across the stress matrix. Diffusivities follow Arrhenius laws relying on mechanism activation energy. They feed the climb velocity and the diffusion-creep contribution introduced in Section 3.

Before loading, the tempered structure contains finite mobile, static, and boundary dislocation densities and a subgrain size set by the heat treatment. As listed in Table 5, the mobile density is measured by TEM in the sample before creep test (as received condition). The static density is assumed as 10 % of the mobile component, which is a standard approximation for tempered martensitic steels. Boundary dislocation density is estimated from EBSD-derived subgrain size and mean misorientation. The initial grain radius is taken from the EBSD result (Section 4.3) and subgrain radius is obtained referring to [36]. These values are applied at $t = 0$ and then evolve through the coupled rate equations.

The glide-annihilation coefficient δ_{anh} (Eq. (9a)–(9b)) is selected as 5 m [50]. The cavitation law uses four calibrated coefficients (see Section 3, Eq. (10) and (13)): $a_d = 0.325$, $b_d = 0.35$, $c_d = 130$ K, and $k_d = 2$.

Table 2
Fixed crystal and elastic parameters.

Symbol	Description	Value	Unit	Source	Appears in
b	Burgers vector	2.48×10^{-10}	m	[46]	Eq. (1), (4), (7)
E	Young's modulus	1.50×10^{11}	Pa	[26]	Eq. (4) (via (G))
μ	Poisson's ratio	0.317	–	[26]	Eq. (4) (via (G))
M	Taylor factor	3	–	[36]	Eq. (1), (4)
Ω	Atomic volume	1.16×10^{-29}	m^3	Calculation	Eq. (6), (7), (9d)
a_g	Lattice constant	2.87×10^{-10}	m	[47]	Eq. (8)

Table 3
Dislocation-structure parameters.

Symbol	Description	Value	Unit	Source	Appears in
α	Dislocation-interaction coefficient	1.0×10^{-2}	–	Calibration	Eq. (4)
c_s	Mobile–static coupling factor	0.4	–	Calibration	Eq. (4), (9a)
β	Dislocation transfer coefficient	3.75×10^{-2}	–	[33]	Eq. (9a)
ζ	Climb geometry constant	3.40×10^{-2}	–	[48]	Eq. (9c)
η_v	Vacancy efficiency factor	2.0×10^{-4}	–	[31]	Eq. (6)
a_1	Glide pre-exponential	5.0×10^{-8}	$m\ s^{-1}$	Calibration	Eq. (3)

Table 4
Activation energy parameters.

Symbol	Description	Value	Unit	Source	Appears in
Q_g	Glide activation energy	4.01×10^{-19}	J	Calibration	Eq. (3)
E_{lattic}	Lattice diffusion energy	2.00×10^{-19}	J	[42]	Eq. (6)
E_{pipe}	Pipe diffusion energy	3.00×10^{-19}	J	[42]	Eq. (7)

Table 5
Initial microstructural state.

Symbol	Description	Initial value	Unit	Source	Appears in
ρ_{m0}	Mobile dislocation density	3.6×10^{14}	m^{-2}	TEM	Eq. (9a)
ρ_{s0}	Static dislocation density	3.6×10^{13}	m^{-2}	Estimation	Eq. (9a), (9b)
ρ_{b0}	Boundary dislocation density	2.2×10^{14}	m^{-2}	Estimation	Eq. (9c)
R_{sgb0}	Subgrain boundary radius	0.1×10^{-6}	m	[36]	Eq. (9c), (9d)
R_{gb}	Mean grain-boundary radius	9.75×10^{-6}	m	EBSD	Eq. (9a), (9b), (9d)

These values were identified once at 550 °C against the measured ductility envelope and the tertiary onset in the creep curves, and then held fixed for all stresses (283–450 MPa). c_d carries temperature units (K); the remaining parameters are dimensionless.

During the calibration of the cavitation parameters, the total creep rate remains decomposed into dislocation and diffusion contributions as defined in Eq. (10). The relative contributions of these mechanisms are not fixed during fitting, but evolve naturally according to the constitutive equations as a function of stress and deformation state. The cavitation parameters primarily control the acceleration of creep through damage evolution and do not modify the partition between the underlying creep mechanisms.

The cavitation parameters are treated as effective material parameters at a given temperature, identified over a defined stress range and assumed to remain valid within this domain. The good agreement between model predictions and experimental creep curves at different stress levels supports the consistency of this assumption.

6. Microstructure data

6.1. Precipitation kinetics

TEM characterization from fractured creep specimens at 550 °C identifies four carbide families in this alloy: Fe_3C, M_6C, $M_{23}C_6$, and MC (Fig. 5, left-bottom). Based on these observations, thermo-kinetic simulations were carried out in Thermo-Calc PRISMA 2025a (TCFE13/MOBFE8) using the measured thermal histories as input. The workflow has two stages. First, the heat-treatment stage (quench, temper, stress-relief) is simulated to establish the initial site distributions and volume fractions (precipitation simulation ①) that enter the creep calculations. The phase diagram and kinetic calculations indicate that $M_{23}C_6$ and MC are not stable at the quench temperature (≈ 900 °C), so the high-temperature step is simplified to Fe_3C and M_6C only. Their fractions at the end of tempering provide the amount of Fe_3C and M_6C. As nucleation is not modelled in TC PRISMA, an initial quantity is inserted based on the equilibrium diagram for the creep simulation run (precipitation simulation ②). Second, the creep stage is simulated at constant temperature (550 °C) under the same nucleation-site hierarchy used in the model (grain bulk, boundaries, edges, corners, dislocations). In this stage, all four precipitate families are included because they are observed in the fractured samples. This means that $M_{23}C_6$ and MC are not neglected in the creep calculations; they are excluded only from the quench-temperature stage of the heat-treatment simulation and are explicitly reintroduced in the creep-stage precipitation simulation at 550 °C. The simulation outputs the time series of mean radius $r_i(t)$ and number density $N_i(t)$ for each precipitate and site; these trajectories are directly supplied to the MFC solver through the effective-velocity and pinning relations.

At 550 °C (precipitation simulation ②), the four carbide families exhibit distinct, site-dependent kinetics, as shown in Fig. 6, and the trends align with thermodynamic stability and diffusion pathways. Fe_3C is transient: its number density rapidly decreases at every sites while the few remaining particles increase in radius, which is the signature of dissolution followed by ripening. This reflects the low stability of cementite in this Cr–Mo–V steel near 550 °C, where $Fe_{33}C$ either dissolves back into the matrix or transforms and thereby supplies solute for later precipitation. A small residual fraction can persist on dislocations because pipe diffusion locally maintains solute supply and temporarily stabilizes larger particles.

It is shown that M_6C displays a rise–fall response during tempering. During the early stage (before 1 h), number density increases as M_6C forms from the tempering inventory and from redistributed solute. With continued holding at 550 °C, both number density and mean radius decline, indicating partial dissolution and turnover toward the phases that are more stable at this temperature. The effect is most pronounced in the grain interior, where nucleation barriers are higher and lattice diffusion limits mass transport. It is also weaker near boundaries where back diffusion and local chemistry promote faster replacement. $M_{23}C_6$ monotonically grows in radius while its number density decreases slowly, which is consistent with classical coarsening. Corner and edge sites show the largest radii, with boundaries following and grain interiors presenting smallest radii. The slower decay in number density at

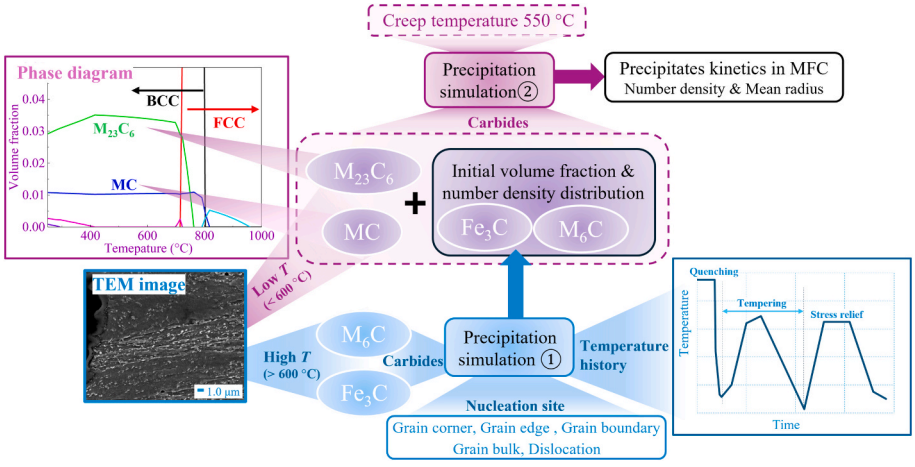

Fig. 5. Flowchart for describing the methodology to perform the thermo-kinetics simulations in TC-PRISMA. TEM confirms Fe_3C, $M_{66}C$, $M_{23}C_6$, and MC in fractured creep specimens of a test at 550 °C, 450 MPa. The heat-treatment simulation ① (quench–temper–stress relief) is used to set initial fractions; $M_{23}C_6$ and MC are suppressed at the quench temperature, so Fe_3C and M_6C are used to initialize the state. A second TC Prisma simulation ② at 550 °C generates $r_i(t)$ and $N_i(t)$ for all four carbides and site levels.

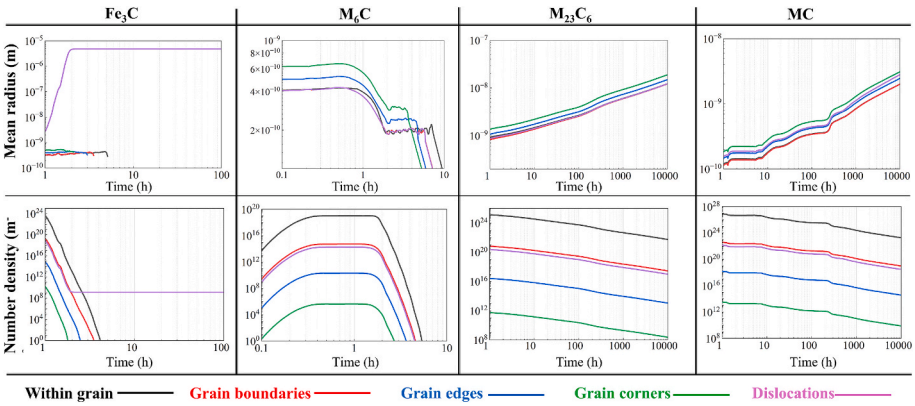

Fig. 6. Precipitate kinetics at 550 °C. Top: mean radius vs time for Fe_3 C, M_6 C, $M_{23}C_6$, and MC at different nucleation sites, i.e., within grain, grain boundaries, grain edges, grain corners and dislocations. Bottom: corresponding number densities.

corners and edges reflects faster mass transport along intersecting boundaries and triple lines, which act as strong sinks and efficient diffusion pathways. MC, which is V rich, also coarsens over time but with comparatively small changes in number density, especially inside grains. Vanadium diffusion at 550 °C is sluggish and MC is stable, so intragranular MC particles grow only slowly and remain nearly constant in number. MC is also present at boundaries, though its primary population resides inside the laths/grains. Where MC is associated with dislocations, radius growth is faster than in the grain interior because pipe diffusion accelerates solute transport along the line defects, which raises the local supply rate to the particle–matrix interface.

Across all species a consistent site hierarchy emerges. Corners and edges develop the largest radii with comparatively gentle declines in number density; boundaries are intermediate, and grain interiors retain higher number densities with smaller radii. Dislocation sites can show rapid early growth or extended survival depending on the balance between pipe diffusion and local depletion. These paired trajectories $\{r_i(t), N_i(t)\}$ directly feed into the constitutive model through the effective dislocation velocity and the pinning length. As the corner/edge and boundary populations of $M_{23}C_6$ coarsen and the intragranular MC population evolves, the dislocation mean free path increases and boundary pinning weakens, which shortens the secondary plateau and promotes the transition to tertiary creep. In the present implementation, the TC-PRISMA precipitation trajectories are introduced into the MFC model through a one-way coupling strategy. The precipitate radii and number densities are precomputed from the thermo-kinetic simulations and then supplied as time-dependent microstructural inputs to the constitutive framework. This does not imply that tertiary creep is assumed to start once precipitates coarsen to a specific threshold. Rather, precipitate evolution remains continuous throughout the creep process, while the onset of tertiary creep emerges from the combined effects of dislocation evolution, progressive loss of pinning, and cavitation damage. Although mechanical effects such as local stress concentration and enhanced dislocation activity during tertiary creep could in principle affect precipitation kinetics, their reverse influence is not treated explicitly here. This approximation is considered reasonable in the present study because tertiary creep occupies only a relatively short part of the total creep lifetime, whereas the main precipitate evolution occurs progressively over the full duration of the test.

For damage calculations we use precipitates on corners, edges, and boundaries, since these locations control boundary pinning and coincide with preferred sites for cavity nucleation and growth. Their coarsening drives the precipitate-damage variable $D_{ppt}(t)$ through the pinning length in Eqs. (11)–(12) and directly contributes to tertiary creep acceleration. For creep hardening we use precipitates in the grain interior and on dislocations as inputs to the effective-velocity law, because these populations set the obstacle spacing for glide and the climb bypass frequency. The pairs $\{r_i(t), N_i(t)\}$ from interior and dislocation sites enter Eq. (2) and shorten or lengthen the mean free path in the Orowan relation, while the corner/edge/boundary sets enter the Zener pinning and damage terms. This separation reflects the physics observed in Fig. 6: interior and dislocation populations dominate rate control, whereas corner, edge, and boundary populations dominate pinning loss and damage onset.

6.2. Dislocation density

Dislocation content was quantified with TEM for the mobile population and with EBSD for geometrically necessary dislocations (GND), so that the simulations start from a measured state with internal representative variables. In thin foils examined at room temperature, line counting with thickness correction gives a mobile dislocation density of 3.6×10^{14} m^{-2}. This value is used as the initial mobile density in the model (Table 4). The same foils show the carbide populations used to scope the precipitation inputs. Representative images of dislocation networks and particle–boundary interactions are shown in Fig. 7. It should be mentioned that independent XRD line-broadening analysis performed on the same heat-treated condition yielded a value of 2.1×10^{14} m^{-2}, which is consistent with typical scatter between electron microscopy and diffraction-based estimations. Since TEM directly resolves individual dislocation lines within bainitic laths, the TEM value is used as the model input, while the XRD result provides supporting confirmation of the order of magnitude.

To characterize lattice curvature and storage after creep, we obtained EBSD maps for three conditions: the as-received specimen, a specimen ruptured at SCT of 550 °C and 450 MPa, and a specimen ruptured at SCT of 550 °C and 283 MPa. Because the fracture plane lies near mid-gauge, sections were taken at fixed distances from the failure and from the grip: position 1, a cross-section 5 mm from the fracture surface, and position 2, a cross-section 10 mm from the raised ring. To characterize lattice curvature and storage after creep, we obtained EBSD maps for the as-received specimen and for two fractured specimens tested at 550 °C, namely 450 MPa and 283 MPa. Because the fracture plane lies near the mid-gauge, two reference cross-sections were defined: position 1, located 5 mm from the fracture surface, and position 2, located 10 mm from the raised ring. For the 283 MPa specimen, EBSD maps were acquired at both positions 1 and 2 in order to compare the near-fracture and far-field regions after long-term creep exposure. For the 450 MPa specimen, only one EBSD map, at position 2, was acquired. This specimen was treated as an extreme high-stress reference case, since 450 MPa is well above the measured yielding threshold and the creep exposure was very short (about 0.8 h before failure). For this reason, a more extensive two-position EBSD survey was not carried out for the 450 MPa case. The 450 MPa EBSD result is therefore used here

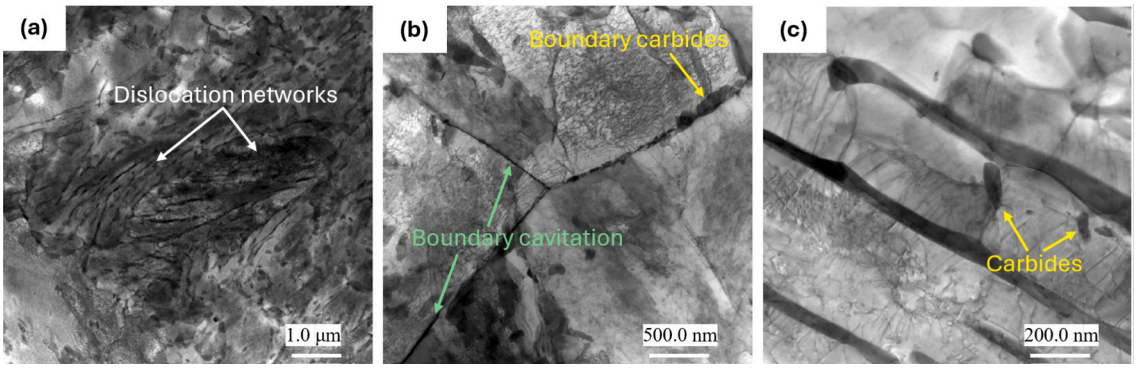

Fig. 7. TEM images at increasing magnification showing representative microstructural features in the heat-treated 30CrMoNiV11-5 steel: (a) dislocation networks, (b) boundary carbides and local boundary cavitation, and (c) carbide distributions within the matrix.

only as a qualitative reference, whereas the location-dependent comparison is mainly discussed for the 283 MPa specimen. Local misorientation fields were computed using a Kernel Average Misorientation (KAM) procedure, and GND density was estimated from the KAM–distance slope within the small-misorientation, Nye-tensor approximation. The resulting misorientation and GND maps, shown in Fig. 8, reveal elevated GND near the fracture side and lower GND in the far field, which is consistent with recovery and subgrain rearrangement during creep. In the model, ρ_{m0} fixes the starting value of the mobile population, while the EBSD-derived GND trends provide qualitative checks on the predicted evolution of $\rho_m(t)$, $\rho_s(t)$, and the subgrain size $R_{sgb}(t)$.

6.3. Effective dislocation-wall spacing

The EBSD surveys provide two complementary microstructure variables that we use differently in the model: an outer grain size from prior-austenite reconstruction, and an internal substructure size associated with low-angle interfaces. The first anchors the specimen geometry and the diffusion length used when dislocation activity is weak. The second controls recovery, mean free path, and the kinetics that govern primary and secondary creep. On the quenched specimen, prior austenite grain size was reconstructed from the EBSD orientation data. From the inverse pole figure (IPF) map together with the combined high- and low-angle boundary map, the prior-austenite grain size (PAGS) is estimated to be about 19.5 μm, as shown in Fig. 9. The reconstruction was carried out using the MTEX 5.9.0 toolbox based on the Greninger–Trojano orientation relationship, and the reported value corresponds to the average equivalent diameter of the reconstructed prior austenite grains. This number should be regarded as indicative. The reconstruction is sensitive to the misorientation cutoff used for boundary picking, to how packets and blocks are merged, and to local banding. Within the reconstructed austenite grains, a dense population of low-angle interfaces appears. These interfaces partition the grains into smaller domains that will act as

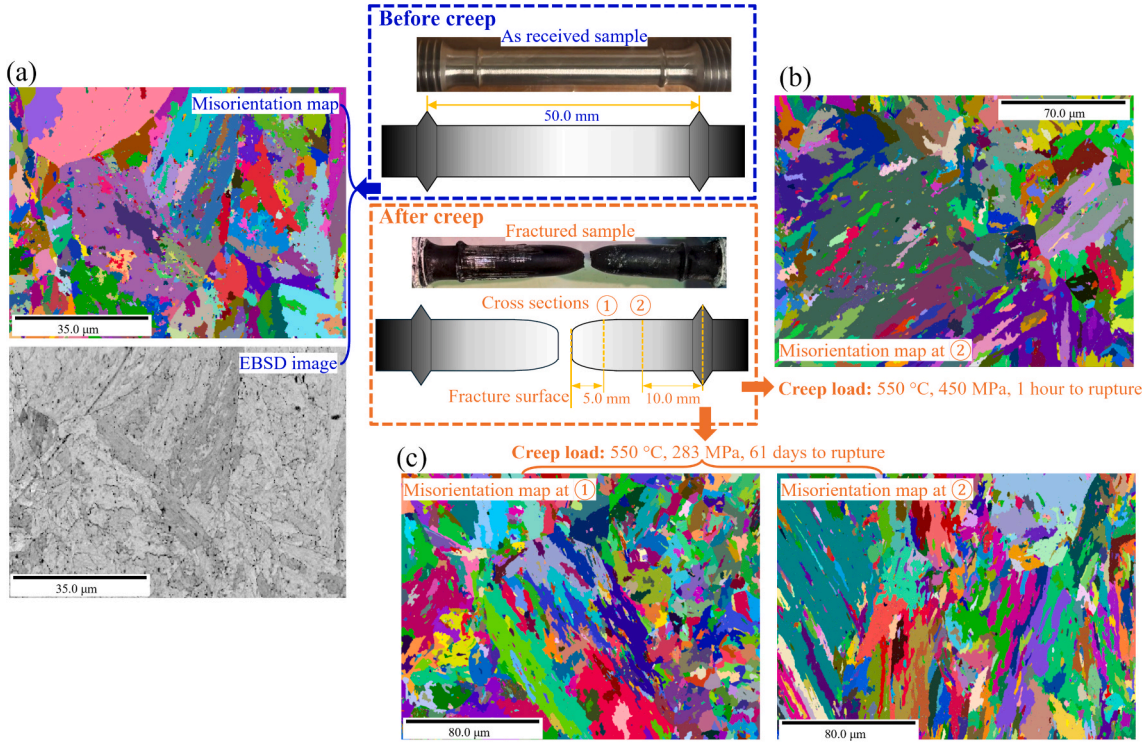

Fig. 8. EBSD overview and KAM-based GND estimation for the (a) as-received state, (b) the fractured specimen tested at 550 °C and 450 MPa, and (c) the fractured specimen tested at 550 °C and 283 MPa. For the 283 MPa case, sections were analyzed at position 1 (5 mm from the fracture surface) and position 2 (10 mm from the raised ring). For the 450 MPa case, only position 2 was analyzed.

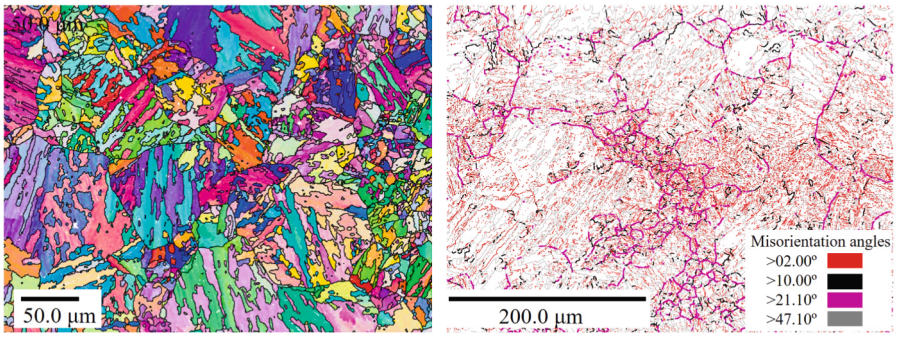

Fig. 9. EBSD of the as-received 30CrMoNiV11-5 material: (a) IPF map and (b) boundary map (high + low angles). Prior-austenite reconstruction gives PAGS ≈ 19.5 µm; the dense low-angle network within larger grains indicates a fine subgrain structure.

dislocation walls during creep.

For the as-received material, EBSD-based area-weighted statistics give a bainitic grain or packet size in the 23–33 µm range for the full field. A zoomed subregion shifts the results toward smaller sizes, as illustrated in Fig. 10. The shift is consistent with the sampling window and with local variations in texture and boundary picking. What matters for MFC modeling is not a single "grain size," but the coexistence of large outer contours with a finer internal network of low-angle boundaries.

Because strain rate during creep is governed by the internal walls rather than the outer grain perimeter, MFC uses an effective subgrain (dislocation-wall) spacing for the dislocation kinetic length. We denote this distance by $R_{sgb}(t)$. The starting value R_{sgb0} is set as a constant that reflects the observed low-angle network, and it is then allowed to evolve through the recovery law in Section 3. Using a constant R_{sgb0} avoids propagating EBSD threshold uncertainty directly into the model while still anchoring the subgrain evolution kinetics to measured microstructure. The PAGS from the quenched state is retained as the maximum dislocation path used for diffusion-creep model and for locating boundary-controlled damage sites, whereas $R_{sgb}(t)$ serves as the internal length that sets the dislocation mean free path, the recovery rate, and the Zener-pinning term. The high-angle contours that define PAG (see Fig. 9) and bainitic packets are structural boundaries with strong misorientation. They bound the transport pathways that become important during late-stage coarsening and for cavity nucleation. The low-angle network inside those contours is the wall system that stores dislocations and accommodates recovery. As creep proceeds, low-angle boundaries migrate and coalesce, which increases $R_{sgb}(t)$. An increasing $R_{sgb}(t)$ lengthens the mean free path, reduces hardening, and raises the weight of diffusion-assisted processes. These trends are consistent with the misorientation and GND patterns reported in Section 5.2.

MFC model uses the measured-informed constant R_{sgb0} for initialization and an evolving $R_{sgb}(t)$ for rate control, while reserving the outer grain scales for diffusion-related terms. This separation keeps MFC simulations tied to the features that actually throttle dislocation motion, and it limits the impact of EBSD threshold choices on the predictions.

7. Results and discussion

7.1. Mechanism split and calibration

Rupture data at 550 °C from our SCT tests (Zwick Roell Kappa 100DS), auxiliary tests through Lukasiewicz-GIT Creep Testing System,

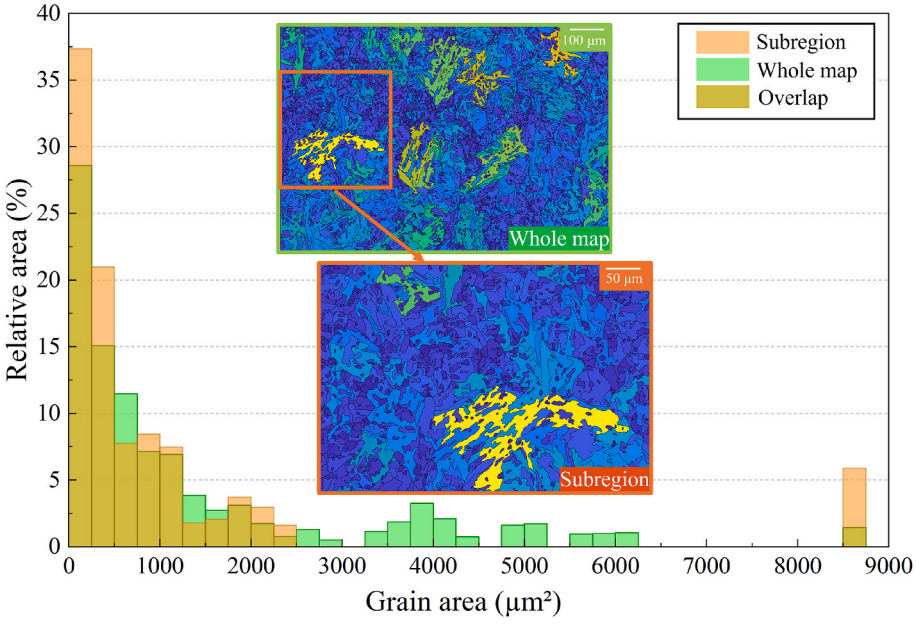

Fig. 10. Area-weighted grain/packet size distribution from EBSD. The grain size across all conditions is generally in the range of approximately 23–33 µm; a zoomed subregion slightly shifts due to local banding. Grain area distribution obtained from EBSD analysis. The darker green regions indicate the overlap between the two distributions due to the use of semi-transparent plotting. (For interpretation of the references to colour in this figure legend, the reader is referred to the web version of this article.)

and literature points were plotted in Fig. 11 using the Larson–Miller parameter $LMP = 10^{-3}T[C + \log_{10}(t_r)]$. Here, C is treated as an empirical fitting constant for the present rupture dataset and was adjusted to obtain the best agreement of the data onto a master curve. In this study, the resulting value is $C = 12.34$. The resulting master curve resolves into two nearly linear branches that intersect between 330 and 360 MPa, with a steeper high-stress branch and a gentler low-stress branch (Fig. 11). This break in slope is consistent with a transition from dislocation-controlled creep at higher stresses to an increasing diffusion share at lower stresses, in line with the Ashby sketch for 550 °C shown with the parameter trends (Fig. 12c).

MFC calibration was first attempted with a formulation in which the diffusion rate followed a fixed Coble-type stress law and no explicit subgrain length was used in the dislocation kinetics (Model 1). The present calibration focuses on the experimental dataset available at 550 °C. Extension of the framework to other temperatures would require additional microstructural datasets to identify the temperature dependence of the governing parameters. In the Coble diffusion term (Eq. (9d)), A_c is taken as a constant and $D_{gb}(T)$ follows an Arrhenius temperature dependence. Fig. 12 summarises the stress-dependent behaviour of the calibrated parameters for the two model variants. Fig. 12(a) corresponds to Model 1, which employs a Coble-type grain-boundary diffusion term and uses the parent grain size (19.5 μm) as the structural length scale. In the lower-stress regime (283–350 MPa), the diffusion-creep prefactor A_c remains nearly constant, while the apparent activation volume V_r increases gradually. This behaviour indicates that only modest adjustments of the glide mobility are required when diffusion contributes appreciably to the measured minimum creep strain rate. Above approximately 350 MPa, close to the measured yielding threshold, the trends reverse. V_r decreases with increasing stress and A_c rises. This sharp increase of A_c reflects the strong stress dependence of boundary-mediated deformation once the material yields. At these high σ/E ratios, boundaries experience intense shear, enhanced vacancy generation and rapid strain-assisted transport, all of which require a larger effective prefactor in the diffusion-related term to reproduce the steep increase in creep strain rate. This behaviour aligns with the limited high-stress experimental evidence available for tempered martensitic steels.

The lower panel of Fig. 12(a) shows the evolution of the tertiary-creep damage parameters A and a_d. Below 350 MPa both parameters remain nearly constant, consistent with limited cavity activity and remarkable precipitate-coarsening effects over the short test durations at 550 °C. Above this stress, the cavity-damage coefficient a_d sharply rises and A approaches its upper bound, indicating that damage initiates very early in the loading and that cavity growth becomes the dominant mechanism controlling tertiary creep and rupture at high stress. Beyond the threshold stress, increasing A has no further effect because damage is triggered immediately at high stress and the initiation point is no longer governed by the SE criterion. Precipitate coarsening remains of secondary importance due to the limited exposure time. Fig. 12(b) presents the calibration trends for Model 2, which incorporates an explicit subgrain length scale ($R_{sgb} = 0.1\,\mu$m) in the recovery and climb terms. In this model we do not apply a Coble diffusion law. Instead, the diffusion-creep strain rate is defined directly to examine how its contribution must vary with stress. With all damage parameters held fixed, the activation volume V_r and the effective diffusion-creep contribution are tuned. Both parameters vary smoothly across the entire stress range. V_r decreases monotonically with increasing stress, while the calibrated diffusion contribution still increases to track the global rise in creep strain rate. This behaviour reflects the balancing required between enhanced dislocation recovery within refined subgrains and the measured minimum-rate curvature.

The parameter trends in both models are consistent with the mechanistic boundary indicated by the Ashby map in Fig. 12(c). Below approximately 330 to 350 MPa, diffusion contributes meaningfully to the rate partitioning, while above this window creep is governed mainly by dislocation glide, climb and cavity-controlled damage. In Model 2 the transition across the stress range is smoother because the diffusion-creep contribution is not restricted to a fixed Coble-type form or to a linear increase with stress. It can rise non-linearly and may grow exponentially at high stress, as indicated in Fig. 12(b). This flexibility allows Model 2 to reproduce the sharp increase in the minimum creep strain rate without altering the damage parameters. In Model 1 the diffusion mechanism is tied to a Coble law and this constraint forces stress-dependent changes in A_c, V_r and the damage parameters in order to match the same experimental behaviour.

7.2. Model–experiment comparison of creep curves

Fig. 13 and Fig. 14 compare the simulated creep curves with the experimental data for the two model variants. Fig. 13 presents Model 1, which uses a prescribed Coble-type grain-boundary diffusion law and no

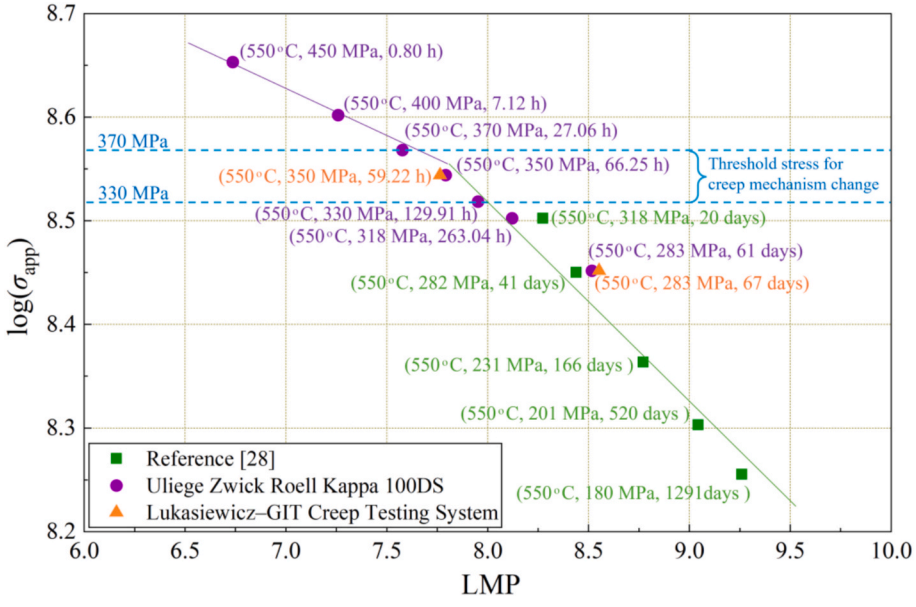

Fig. 11. Larson–Miller master curve at 550 °C with $C = 12.34$; two-segment fit intersects at 330–360 MPa.

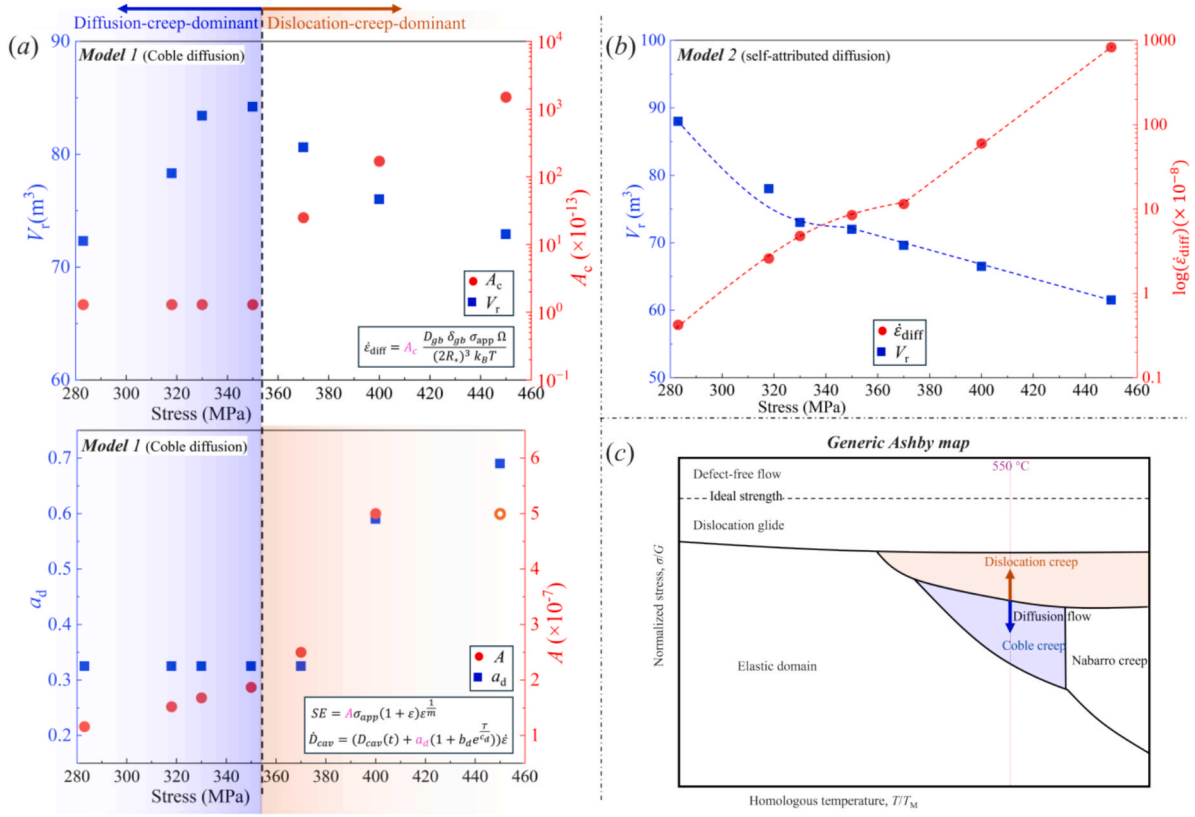

Fig. 12. Calibrated parameter trends at 550 °C. (a) Model 1 (Coble diffusion): stress dependence of V_r and A_c (top) and the damage parameters a_d and A (bottom), showing an abrupt shift above 360 MPa. (b) Model 2 (with $R_{sgb} = 0.1\,\mu$m): smooth variation of V_r and a diffusion-creep contribution identified by inverse modeling. (c) Generic Ashby map indicating the transition from diffusion-driven to dislocation driven creep at 550 °C.

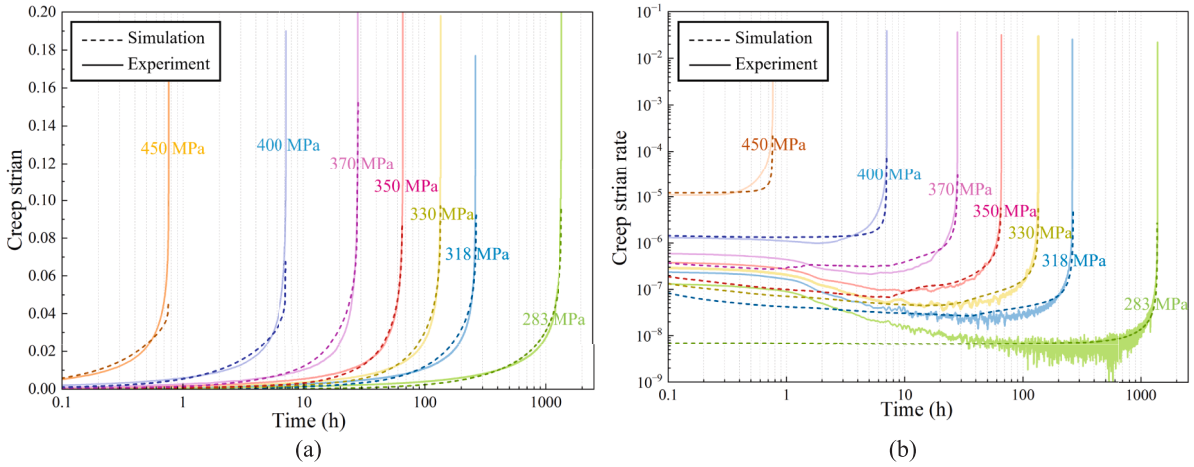

Fig. 13. Predictions of prescribed-diffusion, no-subgrain variant (Model 1, 283–450 MPa) and experiment measurements. (a) Creep strain; (b) creep strain rate.

explicit subgrain length. Fig. 14 presents Model 2, which introduces an explicit subgrain length and defines the diffusion-creep contribution directly rather than through a fixed Coble relation. Panel (a) shows creep strain and panel (b) shows creep strain rate.

Both variants reproduce the three-stage creep response at lower stresses. Model 1 provides reasonable agreement at 318 and 330 MPa, where the primary curvature, the secondary minimum and the onset of tertiary creep fall within the correct ranges. At 283 MPa, however, the very early primary-stage change in creep strain rate is less accurately reproduced. This reflects the fact that the prescribed Coble-type diffusion term used in Model 1 is too restrictive to capture the short initial transient while simultaneously preserving a good description of the minimum creep rate and the long-term curve shape over the full test duration. In the present calibration, priority was therefore given to the overall creep response, including the secondary regime and rupture-related behaviour, rather than to the first few hours of deformation. As the stress increases the limitations imposed by the Cobvariants reproducele formulation become evident. In Fig. 13(b) the model cannot place the initial strain rate and the minimum strain rate simultaneously. Matching the secondary (minimum-rate) plateau forces the initial rate to be too low, while adjusting the initial rate upward distorts the secondary plateau. No single combination of V_r and A resolves this conflict. Once

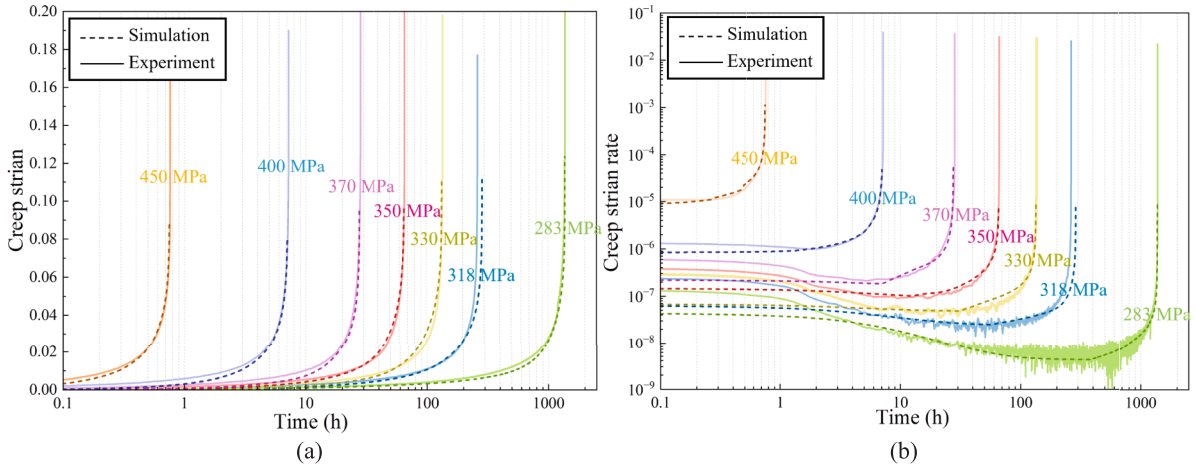

Fig. 14. Predictions of baseline formulation with diffusion fixed from the measured plateau and an explicit subgrain length (Model 2, 283–450 MPa) and experimental measurements. (a) Creep strain; (b) creep strain rate.

the material yields, the measured creep rate rises much more steeply and boundary-mediated deformation becomes strongly stress assisted. Vacancy generation, boundary shear, rapid recovery and early cavity activity contribute to a stress dependence that cannot be reproduced by a linear Coble scaling. For this reason the prescribed-diffusion structure of Model 1 does not remain valid at the highest level of stress.

Model 2 provides a more adaptable representation. The diffusion-creep contribution is directly defined and is not restricted to a linear or fixed stress dependence. It can increase non-linearly and may rise sharply at high stress; however, this behaviour should not be interpreted as a dominance of classical diffusion creep mechanisms, but rather as the response of an effective contribution capturing additional deformation and damage-related processes. In Model 2, the additional diffusion-related contribution is not formulated from a specific governing equation such as Coble or Nabarro–Herring creep. Instead, it is introduced as an effective strain-rate term whose stress dependence is directly identified from experimental observations. This term should therefore be interpreted as a phenomenological contribution that complements the dislocation-based framework, rather than as a strictly defined diffusion-creep law. The purpose of this formulation is to provide a continuous description of creep behaviour across stress regimes, especially at low stress, without imposing a predefined mechanism transition. With all damage parameters held constant, the activation volume V_r and the diffusion contribution can be tuned to match both the minimum creep strain rate and the overall curve shape across the full stress range. Fig. 14 shows that the primary response, the secondary minimum and the acceleration to rupture can be reproduced from 283 to 450 MPa using a single damage constant. This behaviour reflects the flexibility of the formulation rather than a statement about the underlying mechanism.

Both variants capture the three-stage creep behaviour at low and intermediate stresses. Model 1 becomes restricted by the linear Coble-type diffusion law and cannot reproduce the early primary curvature and the minimum-rate plateau simultaneously at higher stresses. Model 2 achieves a closer match to the measured curves across the entire stress range because the diffusion share is free to adjust with stress. This does not imply that Model 2 represents a more accurate physical mechanism. It simply provides the flexibility required to describe the strongly stress-assisted behaviour observed at high stress.

7.3. Microstructural sensitivities

Microstructural inputs control how the constitutive terms partition the creep rate and when tertiary begins. In this section the diffusion contribution is held fixed (identified from the secondary plateau), so any change in the curves arises from the dislocation kinetics and from the damage pathway. The 283 MPa case is used for the grain-size study, and the 350 MPa case is used for the nucleation-site analysis.

In Model 1 the relevant structural length is the grain size R_{gb}, taken from the prior-austenite grain or bainitic block structure. Varying R_{gb} produces a clear and monotonic response. Larger grains reduce the accumulated strain and delay rupture, whereas smaller grains increase the strain and advance the onset of tertiary creep (Fig. 15). This behaviour follows from the mean-field equations. Grain-boundary-controlled source and sink terms scale with the boundary-area density, which varies approximately as $1/R_{gb}$. Reducing R_{gb} therefore amplifies boundary-mediated processes in the dislocation-evolution law. At 283 MPa this amplification primarily accelerates the emission and storage of mobile dislocations at boundaries. As a result, the mobile density ρ_m increases, the internal back-stress $\sigma_i \sim \alpha MGb\sqrt{\rho_m + c_s\rho_s}$ rises, and the dislocation creep term $\dot{\varepsilon}_{disl} = b\rho_m v_{eff}/M_T$ grows. Because the diffusion component is fixed by identification, the secondary minimum remains nearly unchanged; only the primary knee and the tertiary acceleration shift with R_{gb}. Larger grains weaken boundary effects, reduce ρ_m, and delay tertiary creep. A realistic grain-size estimate is therefore essential for capturing early hardening and predicting when damage begins to dominate.

The allocation of nucleation sites for precipitate formation influences both the hardening and coarsening-driven damage terms. At 350 MPa, five representative environments were examined: within-grain cores (CO), grain boundaries (GB), grain edges (GE), grain corners (GC) and dislocation lines (DL). These are the common sites at which carbides and carbonitrides nucleate in tempered martensitic steels. The carbide precipitation characteristics are shown in Fig. 6. While the mean radii at these sites are of similar order, the number densities markedly differ. CO exhibits the highest number densities for all four precipitate families, GB–GE form an intermediate band, and GC shows the lowest population. Because the constitutive hardening and damage laws respond to the combined precipitate population through quantities proportional to Nr^3, these differences govern the model behaviour.

In Fig. 16(a) the coarsening-damage nucleation is fixed at GB, GE and GC, and the nucleation site for precipitate hardening is varied. CO and the combined set [CO, DL] give the strongest hardening response and align most closely with the experiment. This matches Fig. 6, where CO consistently carries the highest number densities and therefore dominates the Nr^3-controlled strengthening term. In contrast, assigning hardening nucleation to GB, GE, GC or DL produces curves that lie close to the "no nucleation'' reference, reflecting their much smaller intragranular particle populations. Thus, the hardening contribution is controlled primarily by intragranular precipitates, whereas boundary-

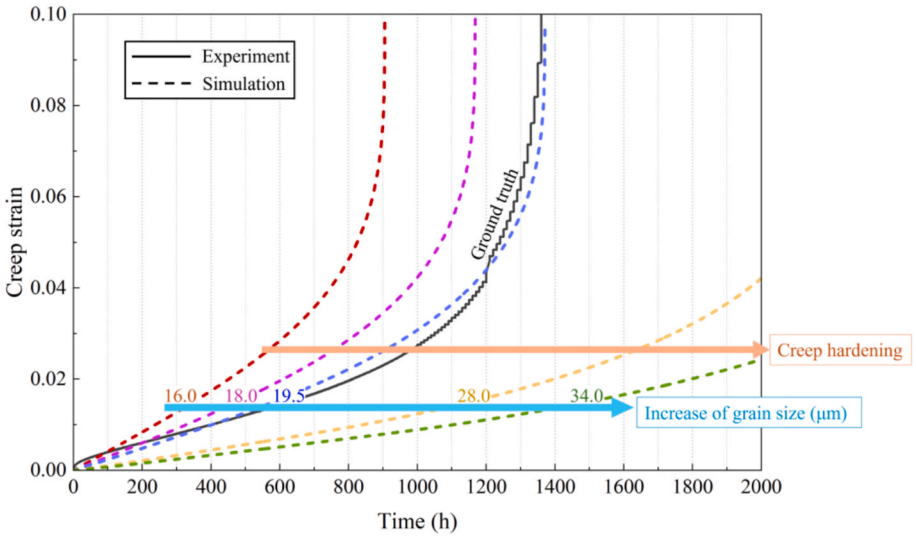

Fig. 15. Sensitivity of the 283 MPa curve (Model 1) to grain size R_{sgb}.

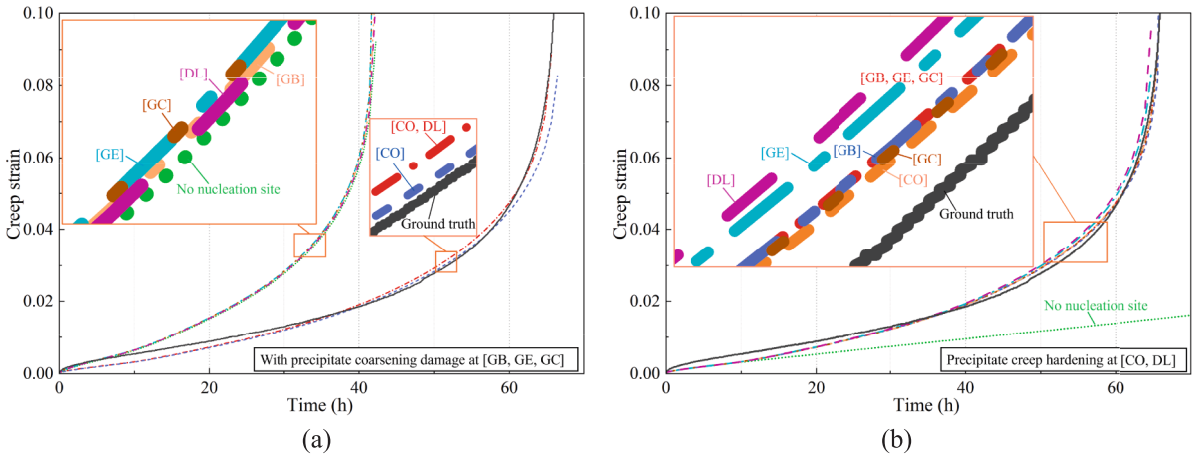

Fig. 16. Sensitivity of Model 1 to nucleation-site choices at 350 MPa, 550 °C. (a) creep strain sensitivity to nucleation sites of precipitates in creep hardening, with precipitates coarsening-damage locations fixed at [GB, GE, GC]. (b) creep strain sensitivity to nucleation sites of precipitates in coarsening-damage, with creep hardening locations fixed at [CO, DL]. CO: within grain core; GB: grain boundary; GE: grain edge; GC: grain corner; DL: dislocation line.

related nucleation has little influence under these conditions.

Fig. 16(b) performs the complementary test by fixing creep hardening nucleation at CO and DL while varying the coarsening-damage nucleation among the five site classes. All nucleation choices except the "no nucleation'' case follow the experimental curve closely. This again agrees with Fig. 6. Although boundary sites differ in number density, their mean radii evolve on similar scales and their combined Nr^3 contributions from the four precipitate families are sufficient to activate the coarsening-damage law at comparable times. Because the creep exposure is only 66 h, precipitate coarsening remains limited, so the differences between nucleation sites are not large enough to produce a measurable shift in the damage response. Assigning coarsening nucleation to GB, GE, GC or even CO therefore produces closely grouped curves. DL and GE produce slightly higher creep strain because their lower precipitate number densities give weaker hardening and allow coarsening-driven damage to develop a little earlier, although the differences remain modest. The only curve that diverges strongly is the "no nucleation'' case, which lacks any precipitate population and therefore cannot build coarsening damage. These trends show that coarsening-driven damage is robust once any realistic boundary environment is activated, and its evolution depends mainly on the shared radius evolution rather than on strong site-specific differences.

Figs. 6 and 16 show that Model 1 response at 350 MPa is driven by the combined Nr^3 contributions from all four precipitate families across the available nucleation sites. Intragranular particles dominate the hardening term due to their high number densities, whereas coarsening-driven damage is relatively insensitive to the precise nucleation boundary site because GB, GE and GC show similar radius evolution and intermediate-to-low number densities. Physically motivated allocations such as [CO, DL] for hardening and [GB, GE, GC] for coarsening remain appropriate, yet alternative choices yield comparable creep curves. The behaviour is governed primarily by the evolution laws and relative precipitate populations rather than by strong local sensitivity to any single nucleation environment.

7.4. Dislocation-density histories and GND

The evolution of the dislocation populations provides a direct view of how the model partitions creep deformation between glide, climb and boundary storage. Fig. 17(a) shows the predicted mobile dislocation density $\rho_m(t)$ for stresses from 283 to 450 MPa. All curves begin at the same TEM-measured initial level of order $10^{14}\,m^{-2}$. At 283 MPa the

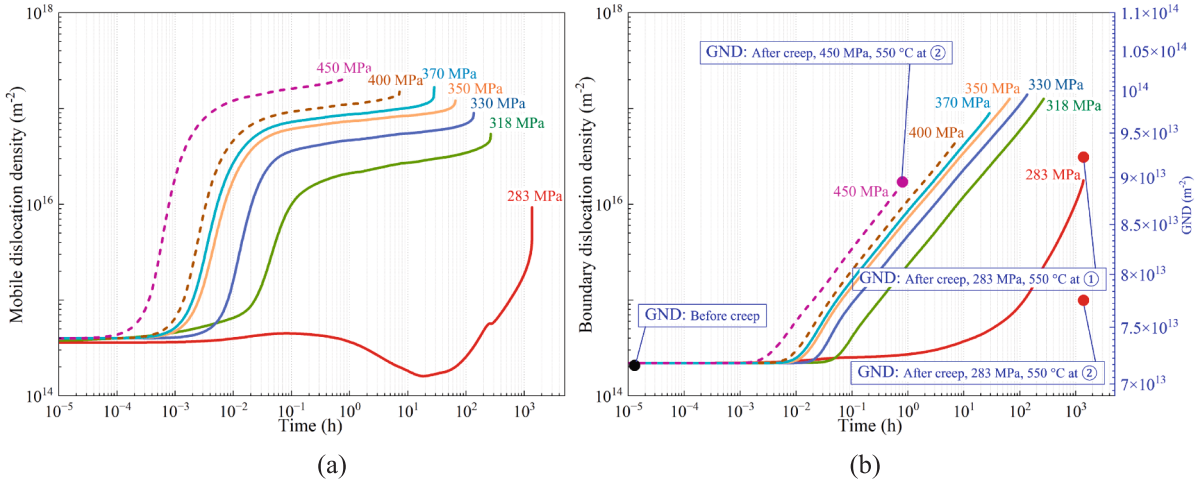

Fig. 17. Predicted evolution of dislocation populations at 550 °C for 283–450 MPa. (a) Mobile dislocation density $\rho_m(t)$. (b) Boundary dislocation density $\rho_b(t)$ (left axis) plotted together with GND benchmarks from EBSD (right axis). "Before creep'' gives the baseline GND. Labels "①'' and "②'' denote EBSD cross-sections taken, respectively, 5 mm from the fracture surface and 10 mm from the raised ring along the gauge of the fractured specimens.

trajectory displays a short primary rise followed by an extended reduction during secondary creep as climb recovery dominates. Only near the onset of tertiary does ρ_m rise again. As the applied stress increases, the behaviour changes systematically: the primary multiplication becomes faster, the secondary plateau shifts upward, and the late-stage growth becomes steeper. Stresses of 318–370 MPa show a clear monotonic build-up during secondary, reaching 10^{15}–10^{16} m^{-2} before acceleration. At 400–450 MPa the multiplication begins earlier and proceeds more sharply, consistent with stronger boundary emission and more rapid storage under higher resolved shear.

Fig. 17(b) shows the corresponding boundary dislocation density $\rho_b(t)$. All stresses start from 2.2×10^{14} m^{-2} and then increase quasi-linearly in log–log space, reaching 10^{16} m^{-2} toward the end of the simulations. Higher stresses produce both higher boundary densities and faster accumulation rates, paralleling the trends seen in ρ_m. The experimentally measured geometrically necessary dislocation density (GND) is plotted on the right axis. The as-received state gives 7.16×10^{13} m^{-2}. After creep at 283 MPa, GND rises modestly to 7.76×10^{13} m^{-2} at position 1 (5 mm from the fracture surface) and to 9.23×10^{13} m^{-2} at position 2 (10 mm from the raised ring). After creep at 450 MPa, the measured GND at position 2 reaches 8.95×10^{13} m^{-2}.

These values lie one to three orders of magnitude below the simulated ρ_b, which is entirely expected. The modelled boundary density represents the full wall/subgrain-boundary dislocation content, incorporating both geometrically necessary and statistically stored dislocations over a subgrain-scale representative volume. In contrast, EBSD GND captures only the curvature-required content at the EBSD step size and therefore provides a lower bound. The comparison is therefore not about absolute equivalence but about qualitative progression. The measured GND increases from the as-received state to the post-creep state at 283 MPa and rises further at 450 MPa, mirroring the monotonic increase of ρ_b with stress. This agreement in trend confirms that the model captures the correct direction and ordering of boundary dislocation evolution across the tested stress range, even though the absolute magnitudes differ by definition and by scale.

8. Conclusion

This work presents a mechanism-based framework for creep-life assessment of 30CrMoNiV11-5 steel, in which a mean-field, dislocation-centred model is coupled with site-resolved precipitate kinetics and damage evolution. The model parameters were identified using a combination of literature values, direct microstructural measurements (TEM, XRD, EBSD), and inverse identification based on creep curves. TC-PRISMA simulations were employed to define both the initial precipitate distributions and their evolution during creep. With this input, the model reproduces the full primary–secondary–tertiary creep behaviour at 550 °C, captures the stress dependence of the minimum creep strain rate, and predicts rupture times across the investigated stress range. The predicted microstructural evolution, including dislocation densities and precipitate trajectories, is consistent with TEM/EBSD observations, supporting the physical basis of the model. The analysis further reveals a transition window near 330–360 MPa between diffusion-influenced and dislocation-dominated regimes. Sensitivity studies clarify the governing mechanisms, showing that dislocation-wall spacing controls the creep rate and tertiary onset, while coarsening-driven damage is mainly associated with boundaries, edges and corners, and intragranular and dislocation-associated precipitates primarily contribute to hardening. Finally, the current limitations include the simplified treatment of diffusion at very low stress and the empirical description of cavitation. Future work will focus on extending the framework to temperature variations, improved damage criteria, and uncertainty quantification for component-level applications.

CRediT authorship contribution statement

Fan Chen: Writing – review & editing, Writing – original draft, Visualization, Validation, Software, Methodology, Investigation, Formal analysis, Data curation, Conceptualization. **Rojas-Ulloa Carlos:** . **Jérôme Tchoufang Tchuindjang:** Writing – review & editing, Resources, Investigation, Data curation. **Olivier Dedry:** Writing – review & editing, Resources, Investigation, Data curation. **Rishabh Bharadwaj:** Writing – review & editing, Resources, Data curation. **Mahesh Somani:** Writing – review & editing, Supervision, Methodology. **Anne Mertens:** Resources, Project administration, Funding acquisition. **Anne Marie Habraken:** .

Declaration of competing interest

The authors declare that they have no known competing financial interests or personal relationships that could have appeared to influence the work reported in this paper.

Acknowledgements

The authors acknowledge financial support from the European

Union's Horizon Europe programme under grant agreement No. 101091912 (AID4Greenest). Anne-Marie Habraken acknowledges support from the F.R.S.-FNRS (Belgium) and the Walloon Region (Belgium). The authors thank Ghent University (UGent) for EBSD datasets; Ilchat Sabirov and Paula Chonillo (IMDEA Materials Institute, Spain) for EBSD microstructure results; Aarne Pohjonen (University of Oulu, Finland) for guidance on microstructure identification; Carlos Llovo Vidal (Reinosa Forgings & Castings) for turbine-shaft heat-treatment data; and GIT (Poland) for experimental support.

Data availability

The experimental and numerical data supporting the findings of this study are available from the corresponding author upon reasonable request.

References

[1] L. Forno, et al., Rotor lifetime assessment: a reference report, in: Dispatchable Technology & Innovations for a Carbon-Neutral Society, ETN Global, 2023, pp. 1–14.
[2] L.M.D.A. Lima, T. Hassan, A novel in situ miniature creep tester for evaluation of new cladding alloys, in: Advances in Materials Technology for Power Plants, vol. 84871, ASM International, 2024, pp. 600–611. https://doi.org/10.31399/asm.cp.am-epri-2024p0600.
[3] ASTM E10-15a, Standard Test Method for Brinell Hardness of Metallic Materials, ASTM International, West Conshohocken, PA, 2015.
[4] M. Godec, D.A. Skobir Balantič, Coarsening behaviour of M23C6 carbides in creep-resistant steel exposed to high temperatures, Sci. Rep. 6 (2016) 29734, https://doi.org/10.1038/srep29734.
[5] M.E. Kassner, Fundamentals of Creep in Metals and Alloys, Butterworth-Heinemann, 2015. https://doi.org/10.1016/C2012-0-06071-1.
[6] F.R. Larson, J. Miller, A time-temperature relationship for rupture and creep stresses, Trans. Am. Soc. Mech. Eng. 74 (1952) 765–771, https://doi.org/10.1115/1.4015909.
[7] G.E. Dieter, D. Bacon, Mechanical Metallurgy, Vol. 3, McGraw-hill, New York, 1976.
[8] F.T. Furillo, S. Purushothaman, J.K. Tien, Understanding the Larson-Miller parameter, Scr. Metall. 11 (1977), https://doi.org/10.1016/0036-9748(77)90164-8 [add page range].
[9] G. Bryndza, J.T. Tchuindjang, F. Chen, et al., Review of the microstructural impact on creep mechanisms and performance for laser powder bed fusion Inconel 718, Materials 18 (2) (2025) 276, https://doi.org/10.3390/ma18020276.
[10] B. Wilshire, P.J. Scharning, A new methodology for analysis of creep and creep fracture data for 9–12% chromium steels, Int. Mater. Rev. 53 (2) (2008) 91–104, https://doi.org/10.1179/174328008X25434.
[11] H. Morch, Thermomechanical modelling of the creep-fatigue behaviour and damage of nickel-alloy receiver tubes used in concentrated solar power plants, Université de Liège, Belgium, 2022. Ph.D. thesis.
[12] Y.N. Rabotnov, A mechanism of the long-term fracture, Voprosy Prochnosti Materialov i Konstruktsii AN SSSR (1959) 5–7 (in Russian).
[13] Y. Liu, S. Murakami, Damage localization of conventional creep damage models and proposition of a new model for creep damage analysis, JSME Int. J., Ser. A 41 (1998) 57–65, https://doi.org/10.1299/jsmea.41.57.
[14] B. Wilshire, P.J. Scharning, Long-term creep life prediction for a high chromium steel, Scr. Mater. 56 (2007) 701–704, https://doi.org/10.1016/j.scriptamat.2006.12.033.
[15] J.A. Cano, C.M. Stewart, Accelerated creep test qualification of creep-resistance using the Wilshire–Cano–Stewart constitutive model and stepped isostress method, J. Eng. Gas Turbines Power 144 (2022) 011016, https://doi.org/10.1115/1.4052205.
[16] J. Wang, Y. Fa, Y. Tian, et al., A machine-learning approach to predict creep properties of Cr–Mo steel with time-temperature parameters, J. Mater. Res. Technol. 13 (2021) 635–650, https://doi.org/10.1016/j.jmrt.2021.04.079.
[17] K. Nakamura, T. Ohnuma, Machine-learning investigation on the creep-rupture time of heat-resistant steels, Mater. Today Commun. 36 (2023) 106687, https://doi.org/10.1016/j.mtcomm.2023.106687.
[18] M. Chai, Y. He, Y. Li, et al., Machine learning-based framework for predicting creep rupture life of modified 9Cr-1Mo steel, Appl. Sci. 13 (2023) 4972, https://doi.org/10.3390/app13084972.
[19] Y. Tan, X. Wang, Z. Kang, et al., Creep lifetime prediction of 9% Cr martensitic heat-resistant steel based on ensemble learning method, J. Mater. Res. Technol. 21 (2022) 4745–4760, https://doi.org/10.1016/j.jmrt.2022.11.067.
[20] J. Sakurai, M. Demura, J. Inoue, et al., Creep life predictions by machine learning methods for ferritic heat resistant steels, ISIJ Int. 63 (2023) 1786–1797, https://doi.org/10.2355/isijinternational.ISIJINT-2023-266.
[21] J.J. He, R. Sandström, J. Zhang, et al., Application of soft constrained machine learning algorithms for creep rupture prediction of an austenitic heat resistant steel Sanicro 25, J. Mater. Res. Technol. 22 (2023) 923–937, https://doi.org/10.1016/j.jmrt.2022.11.154.
[22] L. Holub, J. Dunovský, J. Suchanek, Evaluation of hardness curves of multilayer welds of creep resistant steel 1.6946 using saw method to the ultra narrow gap, Ann. Fac. Eng. Hunedoara 14 (2016) 85, https://doi.org/10.17973/MMSJ.2015_03_201511.
[23] S. Holdsworth, Creep ductility of 1CrMoV rotor steel, Mater. High Temp. 34 (2017) 99–108.
[24] M. Grosso, F. Sansoni, A. Sorce, M. Monti, F. Pascucci, R. Razzoli, Influence of startup management on the residual life of a large steam turbine shaft, in: Proc. ISROMAC 2016, 2016.
[25] F. Kölzow, Application of probabilistic methods for lifetime prediction of high temperature components under creep-fatigue loading, Technische Universität Darmstadt, 2021. Ph.D. thesis.
[26] J. Schemmel, Beschreibung des Verformungs-, Festigkeits- und Versagensverhaltens von Komponenten im Kriechbereich unter instationärer Beanspruchung mit einem elastisch-viskoplastischen Werkstoffmodell, Universität Stuttgart, 2003. Ph.D. thesis.
[27] L. Wei, S. Wang, W. Hao, et al., Prediction of high-temperature creep life of austenitic heat-resistant steels based on data fusion, Metals 13 (2023) 1630, https://doi.org/10.3390/met13091630.
[28] Z. Li, Z. Gan, Phase-field modeling of grain evolution and recrystallization in friction stir processing, in: Proc. Int. Manuf. Sci. Eng. Conf., ASME, 2024, 88100, V001T02A004. https://doi.org/10.1115/MSEC2024-124400.
[29] N.M. Ghoniem, J.R. Matthews, R.J. Amodeo, A dislocation model for creep in engineering materials, Res. Mech. 29 (1990).
[30] S.D. Yadav, B. Sonderegger, M. Stracey, et al., Modelling the creep behaviour of tempered martensitic steel based on a hybrid approach, Mater. Sci. Eng. A 662 (2016) 330–341, https://doi.org/10.1016/j.msea.2016.03.071.
[31] F. Riedlsperger, B. Krenmayr, G. Zuderstorfer, et al., Application of an advanced mean-field dislocation creep model to P91 for calculation of creep curves and time-to-rupture diagrams, Materialia 12 (2020) 100760, https://doi.org/10.1016/j.mtla.2020.100760.
[32] F. Riedlsperger, T. Wojcik, R. Buzolin, et al., Recent progress in the microstructurally based creep modelling of Ni-based alloy 617, Mater. High Temp. 41 (2024) 158–168, https://doi.org/10.1080/09603409.2023.2281123.
[33] F. Riedlsperger, T. Wojcik, R. Buzolin, et al., Microstructural insights into creep of Ni-based alloy 617 at 700 °C provided by electron microscopy and modelling, Mater Charact 198 (2023) 112720, https://doi.org/10.1016/j.matchar.2023.112720.
[34] T. Berecz, P. Jenei, A. Csóré, et al., Determination of dislocation density by electron backscatter diffraction and X-ray line profile analysis in ferrous lath martensite, Mater Charact 113 (2016) 117–124, https://doi.org/10.1016/j.matchar.2015.11.014.
[35] J.S. Dubey, H. Chilukuru, J.K. Chakravartty, et al., Effects of cyclic deformation on subgrain evolution and creep in 9–12% Cr steels, Mater. Sci. Eng. A 406 (2005) 152–159, https://doi.org/10.1016/j.msea.2005.06.029.
[36] T. Zhou, R.P. Babu, Z. Hou, et al., Precipitation of multiple carbides in martensitic CrMoV steels: experimental analysis and exploration of alloying strategy through thermodynamic calculations, Materialia 9 (2020) 100630, https://doi.org/10.1016/j.mtla.2020.100630.
[37] T. Xue, S. Liao, Z. Gan, et al., JAX-FEM: a differentiable GPU-accelerated 3D finite element solver for automatic inverse design and mechanistic data science, Comput. Phys. Commun. 291 (2023) 108802, https://doi.org/10.1016/j.cpc.2023.108802.
[38] Iso, 204, Metallic materials—uniaxial creep testing in tension—method of test, International Organization for Standardization, Geneva, 2018.
[39] J. Kreyca, E. Kozeschnik, State parameter-based constitutive modelling of stress strain curves in Al-Mg solid solutions, Int. J. Plast 103 (2018) 67–80, https://doi.org/10.1016/j.ijplas.2018.01.001.
[40] H. Mughrabi, The α-factor in the Taylor flow-stress law in monotonic, cyclic and quasi-stationary deformations: dependence on slip mode, dislocation arrangement and density, Curr. Opin. Solid State Mater. Sci. 20 (2016) 411–420, https://doi.org/10.1016/j.cossms.2016.07.001.
[41] D. Caillard, J.L. Martin, Dislocation climb, in: Thermally Activated Mechanisms in Crystal Plasticity, Elsevier (2003) 281–307. https://doi.org/10.1016/S1470-1804(03)80038-X.
[42] P.M. Anderson, J.P. Hirth, J. Lothe, Theory of Dislocations, Cambridge University Press (2017). https://doi.org/10.1016/0502-8205(49)90004-0.
[43] D.M. Owen, T.G. Langdon, Low stress creep behavior: an examination of Nabarro–Herring and Harper–Dorn creep, Mater. Sci. Eng. A 216 (1996) 20–29, https://doi.org/10.1016/0921-5093(96)10382-8.
[44] C.Ó. Murchú, S.B. Leen, P.E. O'Donoghue, R.A. Barrett, A physically-based creep damage model for effects of different precipitate types, Mater. Sci. Eng. A 682 (2017) 714–722, https://doi.org/10.1016/j.msea.2016.11.044.
[45] B. Sonderegger, E. Kozeschnik, Particle strengthening in fcc crystals with prolate and oblate precipitates, Scr. Mater. 66 (2012) 52–55, https://doi.org/10.1016/j.scriptamat.2011.10.003.
[46] G.M. Cheng, W.Z. Xu, W.W. Jian, et al., Dislocations with edge components in nanocrystalline bcc Mo, J. Mater. Res. 28 (2013) 1820–1826, https://doi.org/10.1557/jmr.2012.403.
[47] W. Wright, Essentials of Materials Science and Engineering, Cengage Learning, 2019.
[48] F. Abe, T.-.U. Kern, R. Viswanathan (Eds.), Creep-Resistant Steels, Elsevier, 2008.
[49] J. Lemaitre, R. Desmorat, Engineering Damage Mechanics: Ductile, Creep, Fatigue and Brittle Failures, Springer (2005). https://doi.org/10.1007/b138882.
[50] W. Blum, P. Eisenlohr, Dislocation mechanics of creep, Mater. Sci. Eng. A 510 (2009) 7–13, https://doi.org/10.1016/j.msea.2008.04.110.